POLITECNICO DI MILANO

SCHOOL OF INDUSTRIAL AND INFORMATION ENGINEERING

Master of Science in Nuclear Engineering

EXPERIMENTAL STUDY OF A SILICON TELESCOPE FOR MICRODOSIMETRY IN ION-BEAM THERAPY

Supervisor: Prof. Stefano AGOSTEO

Candidate: Sofia COLOMBI
Matr. 836699

Co-supervisors: Dott. Giulio MAGRIN
Prof. Alberto FAZZI

Academic Year 2016-2017

A mia nonna Lina e a mio zio Emi,

che sicuramente saranno in
prima fila a guardarmi.

CONTENTS

Chapter IV. Longitudinal definition of active volume

Chapter V. Transversal definition of active volume

Chapter VI. Radiation damage study

ABSTRACT

Starting with the first patient more than 60 years ago, about 150000 patients worldwide have been treated with proton therapy and carbon ion therapy to date. Detectors able to specify the radiation quality and to correlate it to the effect on the human cells are needed. The peculiarities of the clinical use, in particular the high beam intensity, require to develop new instruments which are substantially different from the microdosimeters regularly used in the framework of radiation protection. One of the most promising devices for this purpose is the silicon telescope developed at Politecnico di Milano.

The aim of this thesis work is to provide further characterization of telescope silicon detectors for its implementation in ion-beam therapy.

The microdosimetric approach to the problem is proposed in *chapter I*, while a discussion of the fundamental microdosimetric quantities is presented in *chapter II*. The chapter focuses also on spectra of lineal energy and how to overcome some distortions of the logarithmic scale representation.

After an introduction in *chapter III* of the operating principles of the silicon telescope and the three different types of detector used in this study, SLAB-0D-1, SLAB-1D and MICRO-DISKS devices, the following sections are dedicated to the experimental analysis performed at the Ruđer Bošković Institute in Zagreb.

The analysis of *chapter IV* provides an estimation of the thickness of ΔE layer of SLAB-0D-1 and SLAB-1D devices, as well as the thickness of the dead layer on the surface. For a correct evaluation of the microdosimetric parameters, the precise sensitive thickness must be known. This evaluation was performed analysing the detector response to different ion probes, carbon, silicon and lithium via IBIC technique, as a function of the incidence angle between the beam direction and the normal to the detector surface.

The purpose of *chapter V* is to estimate the dimension of the border of the detector SLAB-0D-1 and of the small MICRO-DISKS device. The border is defined as the size of

transition between the region where there is a full and homogeneous collection of data and the region where no data are collected.

Radiation damaging studies presented in *chapter VI* investigate the change in the charge-collection efficiency of detector SLAB-0D-1 after exposing it to high fluence rates of 3.616 MeV silicon ions and 15 MeV carbon ions. It is also presented how the charge-collection efficiency was partially recovered after 18 days, during which the detector has been maintained at room temperature.

Finally, the conclusions of the work are presented.

ESTRATTO IN LINGUA ITALIANA

A partire dal primo paziente più di 60 anni fa, ad oggi la radioterapia con protoni e ioni carbonio ha trattato più di 150000 pazienti in tutto il mondo. Pertanto, sono necessari rivelatori capaci di specificare la qualità della radiazione e di correlarla agli effetti sulle cellule umane. Le peculiarità dell'utilizzo clinico, prima fra tutte l'alta intensità del fascio utilizzato, richiede lo sviluppo di dispositivi sostanzialmente differenti dai microdosimetri comunemente utilizzati nell'ambito della radioprotezione. Uno dei dispositivi più promettenti per questo scopo è il rivelatore al silicio a telescopio sviluppato presso il Politecnico di Milano.
Obbiettivo del presente lavoro di tesi è fornire un'ulteriore caratterizzazione di questi rivelatori per il loro utilizzo nell'ambito della radioterapia.

L'approccio microdosimetrico al problema è proposto nel *capitolo I*, mentre una discussione delle quantità microdosimetriche fondamentali è presentata nel *capitolo II*. Quest'ultimo si focalizza in particolar modo sugli spettri di energia lineale e su come risolvere alcune distorsioni legate alla rappresentazione in scala logaritmica.
Dopo aver introdotto nel *capitolo III* i principi di funzionamento di un rivelatore al silicio a telescopio e le tre diverse tipologie di rivelatore utilizzate in questo studio, SLAB-0D-1, SLAB-1D and MICRO-DISKS, i capitoli successivi sono dedicati all'analisi sperimentale condotta presso l'istituto Ruđer Bošković di Zagabria.
L'analisi del *capitolo IV* presenta la stima dello spessore dello strato ΔE per i dispositivi SLAB-0D-1 e SLAB-1D, e del dead layer superficiale. È infatti necessario conoscere in maniera precisa lo spessore del volume sensibile per una corretta valutazione dei parametri microdosimetrici. Questa valutazione è stata condotta analizzando la risposta del rivelatore a differenti ioni ed energie, in questo lavoro sono stati utilizzati carbonio da 15 MeV, silicio da 3.616 MeV e litio da 14.464 MeV, in funzione dell'angolo di incidenza fra la direzione del fascio e la normale alla superfice del rivelatore.
Obbiettivo del *capitolo V* è la stima della dimensione del bordo dei rivelatori SLAB-0D-1 e MICRO-DISKS. Conoscere precisamente le dimensioni del bordo, definito come la dimensione di transizione fra la zona in cui la raccolta di carica è omogenea e

completa e la zona in cui nessun dato è raccolto, risulta quindi di fondamentale importanza per una miglior definizione trasversale del volume sensibile.

Lo studio del danno da radiazione presentato nel *capitolo VI* approfondisce i cambiamenti dell'efficienza nella raccolta di carica del rivelatore SLAB-0D dopo essere stato sottoposto ad alti tassi di fluenza di particelle, nel caso in esame ioni silicio da 3.616 MeV e ioni carbonio da 15 MeV. Viene inoltre mostrato il parziale recupero dell'efficienza nella raccolta di carica dopo 18 giorni, durante i quali il rivelatore è stato conservato a temperatura ambiente.

Infine, vengono presentate le conclusioni del lavoro.

Chapter I

ION- BEAM THERAPY AND MICRODOSIMETRY

1.1 ION-BEAM THERAPY

Every year, more than one million people in the European Union are diagnosed of cancer and it is the second of the most prevalent medical condition after heart-related diseases.

Three are the basic approaches to treat malignant tumours: surgery, chemotherapy, radiotherapy. The first is the widely used method and it's based on the direct removal of the tissues affected by cancer. However, for several reasons including the proximity of the tumor to vital organs and in case of deep seated tumor, it is not always possible. Chemotherapy deals with drugs administering to preferentially tumoral cells and it prevents cells mitosis or causes cells apoptosis. This frequently leads to severe collateral effects related to non-specific actions of the drugs on the cells, creating strong effects on patient. Radiotherapy is the third important player and it involves cancerous cells death by depositing the right amount of energy into the tumoral site. At the current state, all these methods are important actors in the tumor treatment and we need to constantly improve them.

The use of nuclear particles to treat tumors was experimented by the first pioneers during the half of the last century. The first hadrotherapic treatments were carried out with fast neutrons at the Lawrence Berkley National Laboratory (LBLN) since 1930s, followed by the use of protons (1954), helium ions (1957) and neon ions (1979) [1]. Charged particles radiotherapy using proton beams and heavier ion beams, was first proposed for clinical application by R. Wilson in 1946, who recognized that the characteristic curve of energy deposition (the Bragg curve) assures the maximum dose

delivered at the end of the particle path and a low level of dose delivered at the entrance [2]. This allows to treat deep-seated tumors sparing the healthy tissue which surrounds. In Europe, the first proton treatment was successfully carried out at Uppsala (Sweden) in 1954. Seven years later the treatments started at the Massachusetts General Hospital in Boston thank to Boerje Larsson, using the Harvard Cyclotron of the physic laboratory of Harvard University. All these treatments were performed in nuclear physics laboratories adjusted for the purpose. After this first enthusiastic years, it followed a static period broken in the 1900s by the first treatments in hospital facilities: at Loma Linda University Medical Center in California using protons (1991) and at the Institute for Radiological Sciences (NIRS) in Chiba, Japan (1994). Moreover, in 1993 in Switzerland at PSI an important technological new was introduced after a 15-year period of radiobiological research: the first active scanning gantry for 250 MeV protons. Therapy started at the end of 1997 [3].

At present, particle-beam radiotherapy is being performed in about 40 facilities worldwide, the following table shows how many patients have been treated from the very beginning until two years ago, for a total of 154203 treated patients from 1954 to 2015.

Particle	Patient total	Date of Total
He	2054	1957-1992
Other ions	433	1975-1992
Pions	1100	1974-1994
Protons	131240	1954-2015
C-ions	19376	1994-2015

Tab. 1.1 – Particle Therapy Patient Statistics (per end of 2015). Data collected by the Particle Therapy Co-Operative Group.

There are just three dual radiotherapy centers in Europe, which use carbon ions and protons: Heidelberg Ion-Beam Therapy Center (HIT) in Germany, National Centre of Oncological Hadrontherapy (CNAO) in Italy and Ebg MedAustron in Austria.

The tumors eligible for carbon ions radiotherapy are the skull base tumors (chordoma, chondrosarcoma, schwannoma, meningeoma, adenoidcystic carcinoma) and tumors

close to spinal cord (sacral chordoma, chondrosarcoma, soft tissue sarcoma), while the rapidly growing tumors and the metastasizing tumors are not eligible right now.

1.2 ADVANTAGES OF ION-BEAM THERAPY

The advantages of ion-beam therapy compared to traditional radiotherapy include the following aspects:

- Conformity of the dose to the target volume. The conformation of the released dose by the ions used in ion-beam therapy is related to the tumoral shape. The trend of the ionization density to increase the range in water for all the charged particles is called *Bragg curve* and it has a specific peak called *Bragg Peak,* described by William Henry Bragg in 1903: at proximal part the dose is low and almost constant forming the so-called *plateau*, then is evident a quick increase at a well-defined position and finally at the deep (distal) part the beam stops. Therefore, the dose delivered to tissues is maximized over the last few millimetres of the particle's range. Other radiations, like γ-rays, X-rays or neutrons, have a decreasing intensity with depth, and this leads to an additional and unwanted amount of dose delivered to the healthy tissues. To obtain a high and flat dose region in the target able to cover the entire surface of the tumor it's necessary to design what is called a *spread-out Bragg peak* (*SOBP*). Dose profiles in depth for single beam irradiations are compared in the following figure, together with the representation of the SOBP.

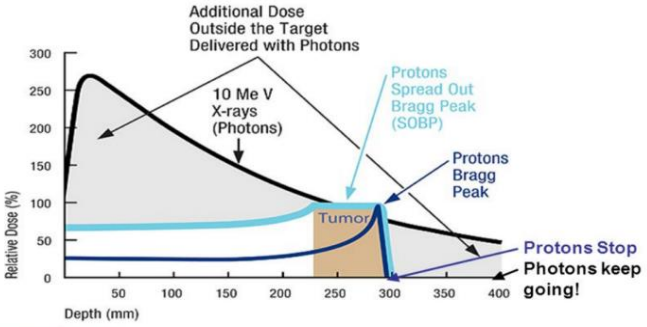

Fig. 1.1 – Charged hadrons dose profile in depth (in water) compared to photons

Two different ways are applied to obtain the SOBP: passive scattering (the old way) and active scanning. The first one works on the principle of scattering between the beam and a dual-ring scatterer (inner foil of high Z material – tungsten or lead – and outsider ring of low Z material – aluminium and lucite). Downstream of a given distance from the dual-ring system, the combined contributions from the inner disk and the external ring give a uniform dose profile, the following figure shows the working principle.

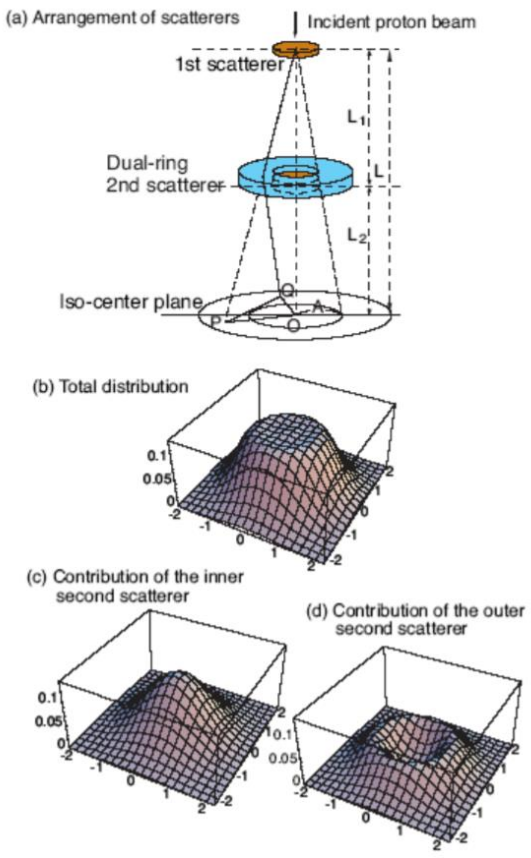

Fig. 1.2 – The"dual-ring scattering system". b) Total dose profile at the isocentre (c+d); c) Contribution from the inner disk of the second scatterer; d) Contribution from the external ring of the second scatterer. From Y. Takada, Nucl. Instrum. Meth. A485 (2002) 255-276.

Downstream of the scatterer is placed a range-modulator specifically chosen to match the thickness of the tumor (a propeller rotating device) which absorbs a variable quantity of energy (i.e. the particle range is varied) and returns a series of Bragg peaks seating at different depths, whose sum is a uniform depth-dose distribution in the target volume, called SOBP.

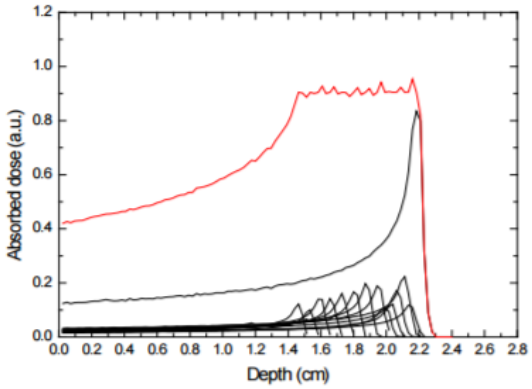

Fig. 1.3 – Modulated Bragg peaks (spread out Bragg peak, SOPB) in a spherical water phantom simulating the treatment of the eye with 50 MeV protons.

In a passive system, the dose is conformed to the target volume through the following devices: the patient's personal collimator and the "bolus". The personal collimator conforms the dose to the target volume shape in the transaxial *x*-*y* plane, while the bolus conforms it in depth.

In active scanning system, small "fancie" beams well defined in energy are moved longitudinally modulating the energy and transversally bending the beam scanning magnets. No collimators, boluses and range modulator are required for active beam distribution.

- The energy release for ions in the cells causes large amount of localized double-strand breaks in DNA. It is important to underline that the ionizations inside the medium are proportional to the absorbed dose and then in principle a certain amount of Gy gives the same number of ionizations, independently on the particle type. But ions produce really close ionizations respect to photons, and the higher the ionization density the higher the probability to create complex double-strand break, which can't be correctly repaired by the cell as in the case of a single-strand break. In comparison to photon and electron beams, the high density of ionization along the penetration path, produced from the high Linear Energy Transfer (LET) of these particles, causes the enhancement of the biological effectiveness of ion beams (Chiriotti Alvatez July 2015).

- The ion beam has a really small diffusion while it penetrates the biological material, because they are heavy particles and this fact reduces the cross section for multiple Coulomb scattering. The consequence is again to better spare healthy tissues.

1.3 LET AND RADIATION QUALITY: THE NEED FOR A MICRODOSIMETRIC APPROACH

The Linear Energy Transfer (LET) is a non-stochastic quantity that includes a series of sub-definitions which specify different conditions. In the field of ion-beam therapy, we assume that when we speak about LET we mean *Unrestricted Linear Energy Transfer* mediated in dose, $L_{\infty,D}$. *Unrestricted* because it's a linear energy transfer with no restriction on the energy of the delta rays released; it describes particle tracks with no limitation of radial extent and it corresponds to the unrestricted electronic stopping power. *Mediated in dose* means that an average is done using as weighting factor the energy (or equivalently the dose) carried by each event. Therefore, the restriction is done with a cut in energy but the meaningful quantity is the space. Only electron collisions are considered, while we are ignoring radioactive effect (Bremsstrahlung), nuclear elastic (Coulomb collisions) and nuclear inelastic processes.
Radiation quality is defined as *the type and energy spectra* of the radiation at a specific point. The Radiation Quality is used to represent the radiation focusing on the way the energy is delivered to the medium: for ions, the energy is densely released and concentrated along the track of the particle, for photons the energy it is more sparsely distributed. Its purpose is to explain why the biological effects on a target irradiated depend also on the characteristics of the radiation other than the dose. For instance, to describe the radiation quality in a small volume of a tumor treated with carbon ions, we should be able to collect the energy spectra of carbon ions, those of each of the ions species resulting from the fragmentation of the primary carbon beam, as well as the spectra of the neutrons and the gamma rays crossing that volume. These measures are

extremely challenging and practically unfeasible. The LET, defined by Zirkle, is considered as a *specification* of the radiation quality and it expresses the heterogeneity of the energy deposition in terms of linear density along the track. The verb *"s*pecify*"* was used the first time sixty years ago by Harald Rossi, when he described his newly invented microdosimeter [4] and it remains today when LET or microdosimetric quantities are used to *"*specify the radiation quality*"* [5]. In 1959 Rossi suggests a specification of the radiation quality based on spectra of lineal energy at different simulated sizes.

One concept represents the link between radiation quality and therapy: the *relative biological effectiveness*, RBE. This is a dimensionless quantity, which estimates how two radiations of different qualities require different doses to produce the same biological effect. Let us consider an example: a certain ion beam is more efficient than Cobalt-60 photon beams in producing cell death, because it needs only 1/3 of the dose of the photon beam to produce the same effect. This is explained saying that the RBE of that ion beam is 3. RBE depends on the radiation quality, on the dose, and on other conditions of the target and the radiation described in details in ref. [6].

Microdosimetric methods are especially useful for high-LET radiation therapy due to the requirement of quantitative specification of radiation quality. For low-LET radiation, absorbed dose is a good predictor of biological effect since the RBE does not vary significantly between X-rays, γ-rays or electrons in the energy range between about 1 to 50 MeV [7] and does not vary with position within the irradiated tissue. Thus, absorbed dose measurements suffice and microdosimetric studies are generally not needed for low-LET radiations.

In contrast, high-LET radiations employing heavier particles (neutrons, protons, heavier ions, negative pi mesons) provide an RBE exceeding unity that may vary significantly with depth and beam parameters such as particle energy. A problem specific to high-LET radiations is the characterization of RBE spatial variation for a given beam compared to photons. Microdosimetric spectrum measurements are a valuable supplement to radiobiological studies in the characterization of RBE. Analytical calculation of RBE is not easily performed, instead empirical approaches have been developed based on calculating parameters from microdosimetric spectrum $y \cdot d(y)$ that correlate with RBE.

Microdosimetric spectra have been extensively used to investigate radiation quality of neutron therapy facilities [7-10]; these results have shown that microdosimetric measurements are capable of discerning subtle changes in the radiation field and provide insight into the interpretation of such changes.

Chapter II

MICRODOSIMETRIC APPROACH

2.1 HISTORICAL REVIEW OF MICRODOSIMETRY

The term *Microdosimetry* originated when Rossi and coworkers (1955) developed conceptual framework and corresponding experimental methods for the systematic analysis of the microscopic distribution of radiation in irradiated matter. The objective of microdosimetry is "to develop concepts which relate some of the principle features of the absorption of ionizing radiation in matter to the size and perhaps the nature of the structure being affected" [1].

The spatial distribution of energy-deposition events has been an essential aspect of most attempts to a quantitative analysis of cellular radiation effects. Target theory in its early form (Desseuer, 1922; Crowther, 1924) dealt with discrete acts of energy transfer, termed *hits*, that were identified with individual ionizations or cluster of ionizations. The spatial correlation of these events was not considered, and target theory in this earliest form could not, therefore, explain the relative biological effectiveness of different types of ionizing radiation. Jordan (1938) was led to the concepts of *concentration effect* and *saturation effect* to explain the dependence of radiobiological yield on *linear ionization density* in particle tracks. The concept of *mean linear ion density* was used independently by Gray (1947). A similar simplified characterization of radiation quality was introduced by Lea in 1946 [12], who used the term *energy dissipation* which was later called *linear energy transfer*, LET, by Zirkle *et al.* in 1952 [13]. The fundamental work of Lea was followed by the work of Howard-Flanders [14], Neary [15] and many others who thought to utilize the ideas of target theory and LET concept (see chapter 1) to explain cellular radiation effects and, as a next step, to use them on the "defective" cells such as carcinogenic cells.

2.2 QUANTITIES AND DISTRIBUTIONS

The complexity of the LET concept [11] and the difficulty of its direct assessment lead to the formulation of a set of stochastic quantities collected experimentally, which provide the fundamental basis for the description of the energy-deposition events in microscopic structure. The measurement of such quantities and their distributions in a well-defined volume is the aim of the experimental microdosimetric methods. In this chapter the principal microdosimetric quantities and concepts are introduced. The formal definitions of microdosimetric quantities are given in ICRU report 36 [11].

The elementary quantity is the *energy deposit* ε_i, which was introduced for the description of the inchoate spatial distribution of energy in charged-particle tracks. ε_i is defined as the energy deposited in a single interaction i.

$$\varepsilon_i = T_{in} - T_{out} + Q_{\Delta m} \qquad (1)$$

where T_{in} and T_{out} are the energies of the incident ionizing particle and the sum of energies of all ionizing particles leaving the interaction (excluding the rest mass), respectively. $Q_{\Delta m}$ are the changes of the rest mass energy of the atom and the all particles involved in the reaction. ε_i is measured in joule or in eV.

The *energy imparted* ε to the matter in a volume is the stochastic quantity

$$\varepsilon = \sum_i \varepsilon_i \qquad (2)$$

where the summation is performed over all energy deposits ε_i in that volume, due to one or more energy deposition events. The expectation value of a stochastic quantity is a non-stochastic quantity. Its value may be estimated as the average of observed values of the associated stochastic quantity. The quotient of ε by m, where m is the mass of the matter in a volume, gives the *specific* (imparted) *energy* z, that is:

$$z = \frac{\varepsilon}{m} \qquad (3)$$

The unit of z is the joule per kilogram, namely *gray* (Gy). z is a stochastic quantity characterized by a probability density distribution f(z). The expectation value, or *mean specific energy*, $\bar{z}$ is defined as

$$\bar{z} = \int_0^\infty z \cdot f(z) \qquad (4)$$

It is a non-stochastic quantity and it is equal to the *absorbed dose* D. This depends on the fact that microdosimetry is typically concerned with volumes that are sufficiently small so that in most types of irradiation the dose can be considered constant [16]. Since $\bar{z} = \mathrm{D}$, the integrand z·f(z) in eq. 4 is the contribution to D delivered between z and z+dz. Thus, it is useful to consider the so-called *dose distribution* of z, d(z), given by

$$d(z) = \frac{z \cdot f(z)}{\bar{z}} \qquad (5)$$

By using the functions f(z) and d(z), two different expectation values, $\bar{z}_F$ e $\bar{z}_D$, can be derived. They are defined as the *frequency average* and the *dose average*, respectively. The quotient of ε_i to $\bar{l}$, where l is the mean chord length in the considered volume, gives *the lineal energy* y_i:

$$y_i = \frac{\varepsilon_i}{\bar{l}} \qquad (6)$$

The unit of lineal energy y is the $J \cdot m^{-1}$, but most commonly, the $keV \cdot \mu m^{-1}$. For a convex body, the mean chord length (defined as the mean length of randomly oriented chords in the volume), is given by Cauchy's theorem, i.e. $\bar{l} = 4V/A$, being A the surface area of this body. y is a stochastic quantity described by the probability density distribution f(y). It is also useful to consider the dose distribution of y, d(y), defined as the fraction of absorbed dose delivered with lineal energy within the interval (y; y+dy).

2.3 EXPERIMENTAL MICRODOSIMETRY USING TEPCs (TISSUE EQUIVALENT PROPORTIONAL COUNTERS)

Microdosimetric measurements deal with the evaluation of experimental quantities closely related to the imparted energy ε. They are typically performed by exploiting the principles of experimental simulation of microdosimetric volumes through proportional counters. The simulation of a microscopic volume of tissue of $1\ g\ \cdot\ cm^{-3}$ is achieved by replacing it by a much larger cavity filled with a tissue-equivalent gas of much lower density. This requires the condition of equivalent energy loss for equivalent trajectories, that is:

$$\Delta E_t = (S/\rho)_t \cdot \rho_t \cdot d_t = (S/\rho)_g \cdot \rho_g \cdot d_g = \Delta E_g \qquad (7)$$

where ΔE_t and ΔE_g are the mean energy losses of a charged particle in a tissue of density ρ_t and in a gas of density ρ_g, while $(S/\rho)_t$ and $(S/\rho)_g$ are the mass stopping powers. d_t and d_g are the track lengths in tissue and in the gas. The equivalence expressed by eq. 7 is verified if the atomic composition of tissue and gas are identical and the stopping powers are independent of the density. The proportional counters conventionally applied in microdosimetry have walls made of tissue-equivalent (TE) plastic and are filled with tissue-equivalent gases (propane-based or methane-based). For ensuring that the secondary particle fluence is independent of density, the atomic composition of the wall and the gas must be identical. This condition cannot always be met in practice. Moreover, the requirement that the mass stopping powers are independent of density is not always fulfilled due to polarization effects in solids (with fast charged particles) [18]. However, tissue-equivalent proportional counters (TEPCs) are the most widely used microdosimeters. They consist of a spherical or a cylindrical gas chamber with a central anode wire electrically isolated from the surrounding chamber walls. The quality of a microdosimetric measurement assessed by a TEPC depends critically on the atomic composition of the filling gas, and in particular on the capability of obtaining gas free from oxygen contamination, that attracts free electrons reducing the gas multiplication. This is particularly difficult,

since the walls in tissue equivalent plastic adsorb the TE filling gas and release electronegative gases (including oxygen). Therefore, the best way of ensuring constant composition is to employ a gas flow system. However, to avoid complications and physical restrictions, counters are frequently employed in a sealed mode operating for days or even weeks (with continuous maintenances). The use of TEPCs for simulating microscopic tissue can lead to distortions of the experimental microdosimetric distribution due to the density difference between the sensitive volume and the surrounding material. The classification and the discussion of these "wall-effects" can be found in ref. [19]. In some particular cases the errors introduced by these effects could not be negligible and it was estimated to be of the order of 10%. The minimization of the "wall-effect" errors was obtained by wall-less counters, by exploiting material grids or field-shaping electrodes to delineate the sensitive volume boundaries instead of solid walls.

Presently, TEPCs represent the reference detectors for microdosimetry because of their sensitivity to low energy particles, and tissue-equivalence. Moreover, a spherical sensitive volume (and similarly a cylindrical volume with height equal to the diameter) is similar to the shape of the cell nucleus, is well defined and independent of the radiation field characteristics (i.e. particle LET, energy, etc.). Unfortunately, these detection systems are complex, expensive and cumbersome.

2.4 EXPERIMENTAL MICRODOSIMETRY USING SEMICONDUCTOR SILICON DETECTORS

The study of semiconductor detectors for microdosimetry dates back to 1980 [20]. The first device employed for this purpose was a 7 μm thick Si(Li) detector irradiated with a beam of negative pions. The results of these measurements were compared to the data acquired with a tissue-equivalent proportional counter simulating a 2 μm thick site. Significant discrepancies were observed, mainly due to the dimensions of the sensitive volume of the silicon detector. Since then, several devices (mainly diodes) coupled to tissue-equivalent (TE) converters were employed for measuring the quality

of radiation therapy beams and for silicon microdosimetry [21-24]. The most attractive feature of a silicon microdosimeter is the possibility to construct devices of micrometric sensitive volume. This characteristic allows to measure physical events in a real micrometric site, differently from TEPCs where the latter is simulated acting on the gas pressure.

Silicon devices can be applied for assessing single-event effects in electronic instrumentation exposed to complex fields around high-energy accelerators or in space missions. The use of micrometric volumes avoids the contribution of wall effects to the measured spectra. Further advantages of such a detector are its compactness, low cost, transportability, low bias voltage and a low sensitivity to vibrations. However, there are some problems concerning the use of silicon devices: the fact that silicon is not a tissue-equivalent material affects both primary and secondary ionizations; the *field-funnelling effect,* which leads to a dependence of the thickness of the zone useful for charge collection on the LET of the impinging particle; the low Signal to Noise ratio, which imposes the minimum detectable energy; the shape and the dimensions of the sensitive zone. Among the items listed above, the field funnelling effect [25] plays a major role. This effect is due to a local distortion of the electric field in the depletion layer, induced by high-LET particles, leading to the collection of electron-hole pairs produced in the non-depleted zone. This effect is responsible for the dependence on LET of the thickness of the sensitive zone and therefore it must not be present in a device applicable for microdosimetry, where this thickness has to be known accurately. Charge confinement inside a micrometric sensitive volume can be obtained with alternative devices, such as the monolithic silicon telescope. This system can be a valid alternative to the TEPCs from a practical point of view, being simple, easy-of-use, transportable, cheap and versatile.

2.5 MICRODOSIMETRIC SPECTRA

The lineal energy distributions are represented in frequency or dose spectra.
As described in the previous paragraph, the *lineal energy* y is a stochastic quantity, defined for single energy-deposition event, and then it is useful to consider its distribution function, F(y), which expresses the probability that the lineal energy is equal to or less than y. The relating probability density, f(y), is the derivative of F(y) with respect to y and it's also called *lineal energy distribution*:

$$f(y) = \frac{dF(y)}{dy} \qquad (8)$$

It represents the spectrum in frequency and the integral of this function between two values of lineal energy is proportional to the fraction of the total events that have lineal energies included between that two values.
These quantities are used to derive the *frequency-mean lineal energy* $\bar{y}_F$ as follow:

$$\bar{y}_F = \int_0^\infty y \cdot f(y)dy \qquad (9)$$

Analogously, the spectrum in dose is represented by the *dose probability density*, d(y), which is defined as the derivative of D(y) with respect to y, where D(y) is the *dose distribution* of d(y), i.e. the fraction of absorbed dose delivered with lineal energy lower than or equal to y.

$$d(y) = \frac{dD(y)}{dy} \qquad (10)$$

It can also be defined starting from $\bar{y}_F$ as

$$d(y) = \frac{y \cdot f(y)}{\bar{y}_F} \qquad (11)$$

It is finally possible to derive the *dose-mean lineal energy* $\bar{y}_D$:

$$\bar{y}_D = \frac{1}{\bar{y}_F} \int_0^{\infty} y^2 \cdot f(y) dy \qquad (12)$$

F(y) and D(y) are probabilities, then F(0)=0, D(0)=0 and F(∞)=1, D(∞)=1:

$$\int_0^{+\infty} f(y) \cdot dy = \int_0^{+\infty} \frac{dF(y)}{dy} dy = \int_0^{+\infty} dF(y) = F(y)\Big|_0^{+\infty} = 1 \qquad (13)$$

$$\int_0^{+\infty} d(y) \cdot dy = \int_0^{+\infty} \frac{dD(y)}{dy} dy = \int_0^{+\infty} dD(y) = D(y)\Big|_0^{+\infty} = 1 \qquad (14)$$

Since the ranges of lineal energy values may vary over five orders of magnitude for a common radiation field, microdosimetric spectra are usually shown in a semi-logarithmic representation, i.e. by using a logarithmic scale for the abscissa values y, rather than a linear plot. The adoption of this type of scale allows to better appreciate, with a single distribution, the complex spectral components. For ion-beam therapy the logarithmic representation is useful because the values of lineal energy vary consistently between high and low beam energies and the spectra extend to large lineal energy interval at the end of the range.

In order to preserve the probabilistic meaning of the areas displayed in the spectra, referring to the probability density function, a y·f(y) vs log(y) representation is adopted. In fact:

$$\int_{y_1}^{y_2} f(y) \cdot dy = \ln 10 \int_{y_1}^{y_2} [y \cdot f(y)] d \log(y) \qquad (15)$$

and therefore switching to a logarithmic representation the area delimited by y_1 and y_2 maintains the same information. By applying the same principle, dose distributions are plotted by using a y·d(y) vs log(y) representation.

From a set of experimental data of the lineal energies collected for a specific radiation field it is possible to correlate f(y) and d(y) to the estimated value from experimental data $f(y_i)$ and $d(y_i)$. The step function $F(y_i)$ is easily computed, for the i-th step,

dividing the number of all the events with lineal energy below the value y_i by the total number of events.

The probability density function f(y) can be approximated by the function $f(y_i)$:

$$f(y) = \frac{dF(y)}{dy} \cong \sum_{i=0}^{\infty} \frac{\Delta F(y_i)}{\Delta y_i} = f(y_i) \qquad (16)$$

We can use this function to evaluate the frequency mean linear energy

$$\bar{y}_F = \int_0^{\infty} y \cdot f(y) dy \cong \sum_{i=0}^{\infty} y_i \cdot f(y_i)\, \Delta y_i \qquad (17)$$

Analogously to $F(y_i)$, we can build a function $D(y_i)$ wich approximates the distribution D(y) and we can define $d(y_i)$.

$$d(y) = \frac{dD(y)}{dy} \cong \sum_{i=0}^{\infty} \frac{\Delta D(y_i)}{\Delta y_i} = d(y_i) \qquad (18)$$

And again, the *dose-mean lineal energy* $\bar{y}_D$ results:

$$\bar{y}_D = \frac{1}{\bar{y}_F} \int_0^{\infty} y^2 \cdot f(y) dy \cong \frac{1}{\bar{y}_F} \sum_{i=0}^{\infty} y_i^2 \cdot f(y_i) \Delta y_i \qquad (19)$$

The constant that links the experimental $f(y_i)$ and $d(y_i)$ is the value $1/\bar{y}_F$:

$$d(y_i) = \frac{1}{\bar{y}_F} \cdot y_i \cdot f(y_i) \qquad (20)$$

Both spectra, f(y) and d(y), can be represented referring to linear increments on both axis. However, a common way of representing d(y) is via semi-logarithmic plot.

To switch to a semi-logarithmic representation, it is necessary to evaluate the experimental data in discrete points obtained by dividing the abscissa in logarithmic intervals N, typically 40 or more per decade. The rebinning of linear spectra on a logarithmic scale is achieved by assigning to a given i-th logarithmic interval the sum of counts from the linear spectra registered in this interval.

The i-th logarithmic limits is computed as

$$y_i = 10^{\frac{i}{N}}, \qquad i = 0{:}\,1000 \qquad (21)$$

$$\Delta y_i = y_i - y_{i-1} \qquad (22)$$

i.e. Δy_i is the difference between two consecutive logarithmic limits.

We also introduced y_j that is the mean logarithmic value, obtained with the following expression:

$$y_j = 10^{\frac{i-0,5}{N}} \qquad (23)$$

The first model considers the definition of $f(y_i) = \frac{\Delta F(y_i)}{\Delta y_i}$ and uses the logarithmic increments Δy_i and a value of $\Delta F(y_i)$ obtained by adding all the linear channels contained between the lower and the upper limit of a logarithmic interval.

The second model asses the value of $d(y_k)$ from the linear collection of values associating to the j-th mean logarithmic value the closest evaluation of $y_k \cdot f(y_k)$ from the data linearly spaced.

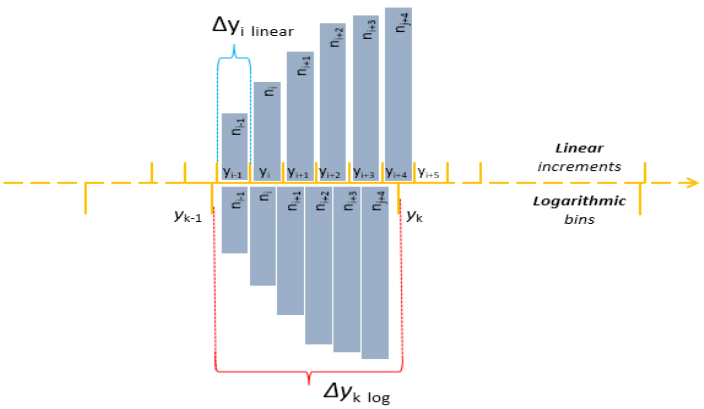

Fig. 2.1 – Illustration of how the experimental data can be grouped in lineal increments (on the top) or in logarithmic increments (on the bottom). The first method evaluates $f(y_i)$ using increments Δy_i as those displayed in the bottom part of the figure. The second method evaluates $f(y_k)$ using increments Δy_k as those displayed in the top part of the figure.

If the statistics is good the two representations lead to functions that well overlap and are close to each one, since $f(y_{i-1}, y_i) \cong f(y_{k-1}, y_k)$. This is not the case if the statistic is poor.

The values of $\bar{y}_D$ and $\bar{y}_F$ obtained with the two representations can be used numerically to compare representation by changing the number of bins per decade and see the deviations respect to the reference value of the same quantities obtained with a linear representation of $f(y_i)$ and $d(y_i)$.

As an example, for a 774 MeV carbon ion beam entering a diamond detector, 2 μm in thickness and 3,52 $g \cdot cm^{-3}$ in density, and developing the logarithmic model with 1000 logarithmic intervals and a variable number of channels to consider in a single logarithmic interval varying from 10 to 70. From figure 2.2 we can see how the $\bar{y}_D$ and $\bar{y}_F$ values computed with the first method are more stable and closer to the reference values compared to the one computed with the second method.

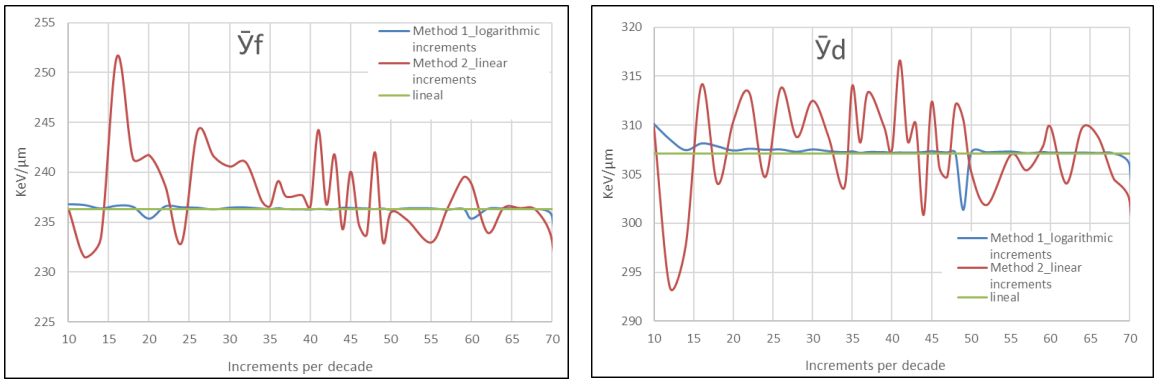

Fig. 2.2 – Values of $\bar{y}_D$ and $\bar{y}_F$ obtained with the linear model (constant green line), with the logarithmic increments method (blue line) and with the linear increments method (red line).

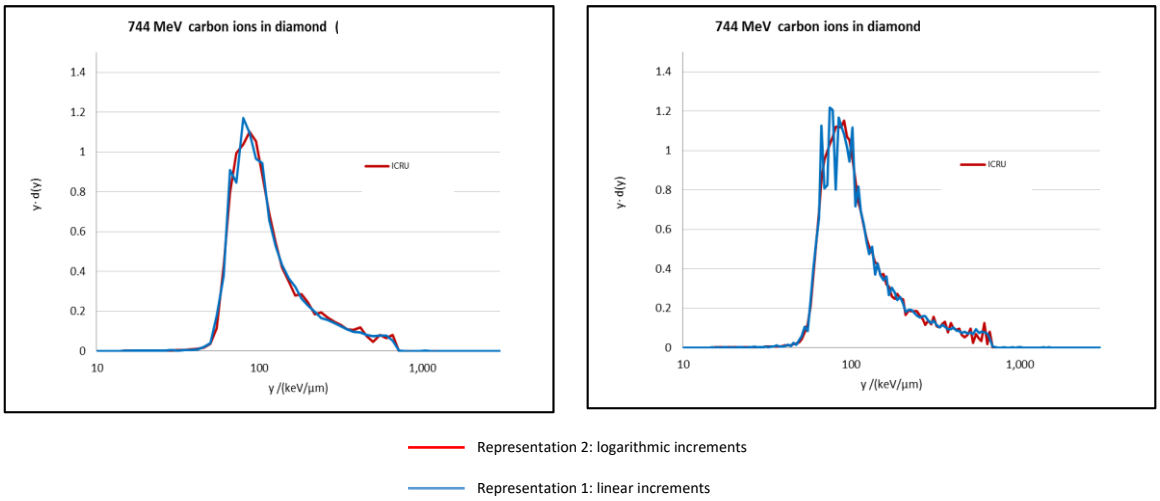

Fig. 2.3 – Logarithmic microdosimetric spectra of 774 MeV carbon ions beam in diamond, considering 25 bins per decade on the left and 60 bins per decade on the right: representation number one with linear increments in blue line, representation number two with logarithmic bins in red line.

	Evaluation from the linear distribution	Linear increments		Logarithmic increments	
		25 bins	60 bins	25 bins	60 bins
$\bar{y}_F$ (keV · µm^{-1})	112.52	113.88	113.85	112.51	112.57
$\bar{y}_D$ (keV · µm^{-1})	157.26	156.60	154.19	155.87	156.07

Tab. 2.1 – Comparison between $\bar{y}_F$ and $\bar{y}_D$ values obtained with a linear approach and both the logarithmic approaches presented for 25 and 60 bins per decade.

It should be noted that the second model is much better than the first one for a low lineal energy value and when the variation is steep, due to small fluctuations. But it is evident that modifying the number of bin per decade the fluctuations change the position and therefore they don't have any real physical meaning, but just the result of a poor representation. This can be explained by noticing that the density of logarithmic bins is high compared to the density of channels: few channels, and in extreme cases no channels at all, are put together in a single logarithmic bin. In these circumstances the number of channels contained in consecutive logarithmic bins can change drastically, as it's shown in the following figure.

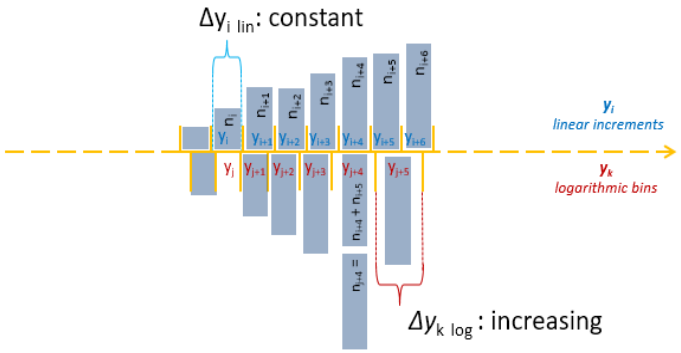

Figure 2.5 – High density of logarithmic increments (bottom figure) can produce high fluctuations in d(y). This can affect the representation 1 used at low values of lineal energy.

On the other hand, at high values of lineal energy the fluctuations are more evident for the second representation. This is correlated to the fact that at high lineal energy these representations use the information of a single linear channel, so while tens or possibly hundreds of channels are collected, the single logarithmic bin and most of the experimental information is therefore waisted. At the contrary representation one uses all available experimental data and the incremented statistic reduces the uncertainty.

In conclusion, in order to represent spectra of lineal energy in a way that is less dependent on the experimental parameters (as the energy difference between the channels in the multichannel analyser and a low collection statistics) an experimental solution is to increase the density of the channels in the multichannel analyser. If this is not possible the suggestion is to use a combined representation of the spectrum $y \cdot d(y)$ mixing both methods, choosing the second representation for small value of lineal energy, the first representation for high values of lineal energy, and choosing a transition point from the visual representation of the two spectra, a in the following representation [26].

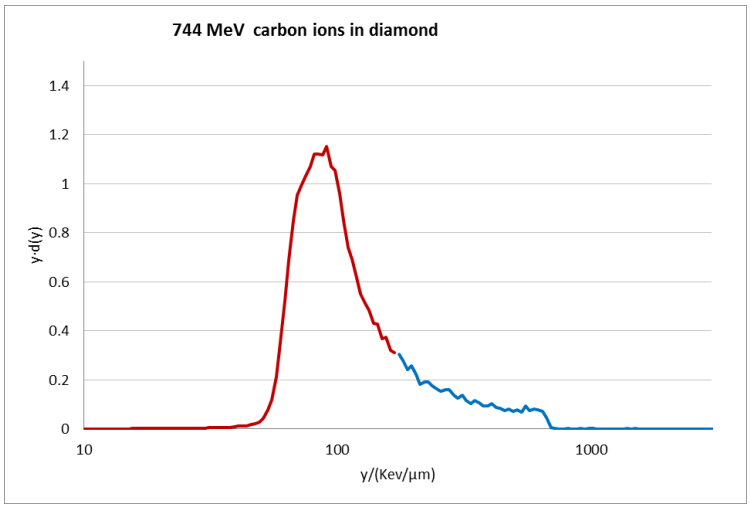

Figure 2.5 – Mixed y·d(y) spectra combining representation two for small value of lineal energy and representation one for high values of lineal energy.

It's important to point out that this approach is suggested only for the representation of the spectra and not for the evaluation of the moments $\bar{y}_D$ and $\bar{y}_F$. Although it's possible to evaluate $\bar{y}_D$ and $\bar{y}_F$ using the logarithmic, the more correct way is to use the linear representation where no-rebinning and consequently no approximation is done.

2.6 THE PECULIAR CHARACTERISTICS OF MICRODOSIMETRY FOR ION-BEAM THERAPY

The characteristics of the proton beam used in radiation therapy at MedAustron are the following: a full width at half maximum, FWHM, at the isocentre for energy of 252MeV of 4 mm, dose delivered to the patient from one portal in one fraction of approximately 0.9 Gy, a spill length of 5 seconds and a total number of protons per spill of 10^{10} particles. From these values, we can estimate a proton fluence rate of the order of 100 protons $\cdot$ µm^{-2} $\cdot$ s^{-1}. The physical size of the cross section of the detector must be chosen by referring to the fluence rate in order to avoid signal pile-up, which happens when pulses arrive closer in time than the pulse resolution time of the system.

Another characteristic of the ion therapy beams is that they are nearly unidirectional throughout most of the path within the target. This means that the sensitive volume used can show unequal elongations of the transversal and longitudinal dimensions if the orientation of the detector toward the beam is correctly assessed.

Finally, in most of the radiation fields investigated in the framework of radiation protection the quality of the radiation is *a priori* unknown. This is not the case in radiation therapy where, in each point of the irradiated volume, the radiation quality is reasonably known for the fraction of radiation delivered by primary particles. In particular, at the entrance of the irradiated volume the radiation quality is completely defined with high precision as the beam is composed exclusively of primary particles (the contribution from nuclear interactions on vacuum window and on air is small and the "contamination" from neutron and gamma radiation consists to approximately 0.1% of the primary dose [28]). These conditions make studying the radiation quality in ion beam therapy substantially different from the approach adopted in radiation protection.

Chapter III

MONOLITHIC SILICON TELESCOPE

3.1 OPERATING PRINCIPLES

The usefulness of semiconductors for radiation measurement stems from the special properties created at a junction where n- and p-type semiconductors are brought into a good thermodynamic contact. The p-n junction represents the surface that separates the two detector zones subjected to different quantities of dopant material. The p-n junction is made by a zone with a large concentration of electrons (n layer) and a zone with a large concentration of holes (p layer). In the case of the present work the concentration difference is obtained through Boron implantation ($\sim 10^{18}$ atoms $\cdot\ cm^{-3}$). If the additional trivalent impurity occupies a substitutional site, it has one fewer valence electron than the surrounding silicon atoms and therefore one covalent bond is left unsaturated. This vacancy represents a hole similar to that left behind when a normal valence electron is excited to the conduction band. Therefore, these *acceptor impurities* also create electron sites within the normally forbidden energy gap. In this case the acceptor levels lie near the bottom of the gap between valence band and conduction band because their properties are quite close to sites occupied by normal valence electrons. Normal thermal excitation on the crystal ensures that there will always be some electrons available to fill the vacancies created by the acceptor impurities or to occupy the acceptor sites. Because the energy difference between typical acceptor sites and the top of the valence band is small, a large fraction of the acceptor sites is filled by such thermally excited electrons. These electrons come from other normal covalent bonds throughout the crystal and therefore leave holes behind in the valence band. To a good approximation, an extra hole is created in the valence band for every acceptor impurity that is added [18].

A space charge region, called *depletion region*, exists in correspondence with the p-n junction and it is similar to a *diode*. This region acts like a high resistivity parallel-plate ionization chamber making the detector feasible to use for radiation detection. The high electric field in this region separates electron-hole pairs formed by ionizing radiation crossing the detector volume and collects the carriers via drift. At room temperature, the mean energy per electron-hole pair (W) is 3,62 eV based on alpha-particles measurements. This is about 10 times lower than for a gas detector. The value of W varies with particle type and energy. The rapid movement of carriers in the electric field generates a current pulse at the device electrodes. By applying a reverse bias to the p-n junction, the charge collection capabilities of the device may be improved [28].

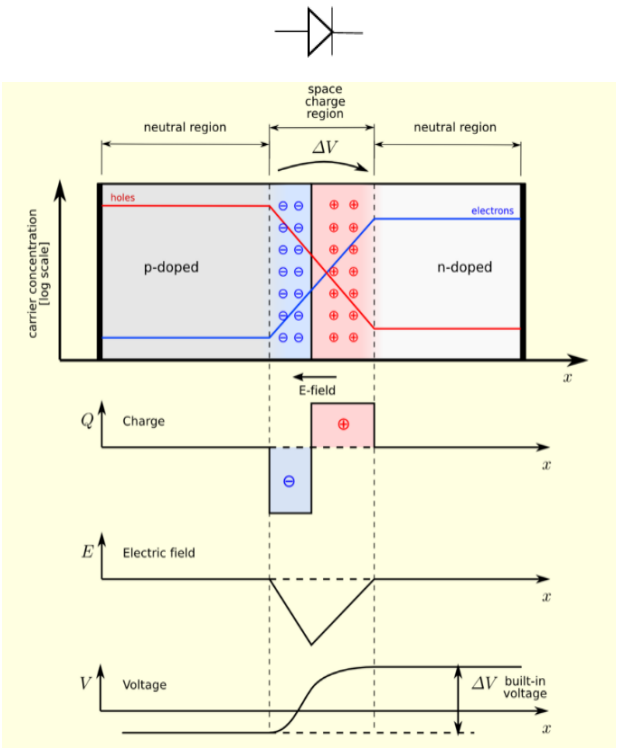

Fig. 3.1 – a. p-n junction scheme; b. Charge density for the step PN junction under the depletion approximation; c. Electric field across step PN junction for charge distribution in b; d. Electric potential variation across PN junction for field in c.

The majority carriers diffuse in the zone with less concentration, therefore minority concentrations increase at the edges of the space-charge region. The non-equilibrium concentration can be expressed as a function of thermal equilibrium concentration and exponential trend of the applied voltage V_a:

$$n_p(x_p) = n_{p0}\left[e^{q\frac{V_a}{K_B T}} - 1\right] \qquad (1)$$

$$p_n(x_n) = p_{n0}\left[e^{q\frac{V_a}{K_B T}} - 1\right] \qquad (2)$$

Where n_{p0} is the electron density at the edge of the neutral p-zone in the thermal equilibrium case, which is equal to the electron density inside the neutral p-region in the non-equilibrium case (n_p) far away from the edge (similarly for p_{n0} and p_n); considering Boltzmann constant, K_B , and q fundamental charge value, the expression $\frac{q}{V_B T}$ is also defined as thermal voltage V_t.

The *built-in* voltage (V_{bi}) represents the voltage created at the p-n junction border, under electrostatical equilibrium condition and without any other external applied voltage. When a forward bias is applied, the voltage across the junction decreases from the equilibrium value V_{bi} by the externally applied voltage V_a (figure 3.2). In thermal equilibrium, the Fermi level, which represents the energy level corresponding to an occupation probability of 0.5, is constant across the entire structure and the built-in electric field opposes to the diffusion of carriers across the junction. The applied bias is assumed to drop almost entirely across the depletion layer and thus the Fermi level becomes separated by a quantity q · V_a. Forward bias reduces the built-in electric field and thus the built-in potential barrier is reduced by V_a as shown. Reverse bias on the other hand increases the built-in electric field and the built-in potential is increased by a quantity V_a.

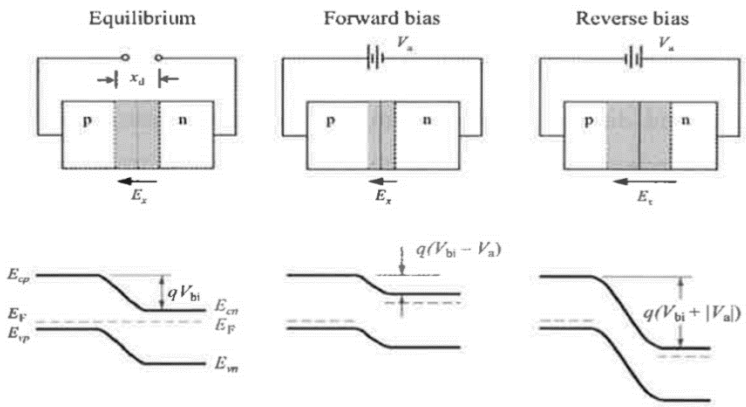

Fig. 3.2 – Effect of applied bias on PN junction (with similar doping levels on either side).

Because the minority diffusion currents are proportional to the deviation of the minority carrier concentrations from their equilibrium values at the boundary, it means that they have an exponential dependence on voltage (Lutz 1999). This can be expressed by the following Shockley equation:

$$J = J_s \left[e^{q\frac{V_a}{K_B T}} - 1 \right] \qquad (3)$$

J_s is the reverse bias saturation current density and it can be calculated by solving the time independent continuity equation for minority carriers with the boundary condition of zero minority carrier concentration at the edge towards the space-charge region. If dimensions of the silicon wafer are very small, little recombination occurs in the bulk of n- and p-type regions, therefore exponential trend is interrupted and the concentration is forced to zero at the contact with neutral zone, because recombination is complete at the contact surface. This situation is described as short-base diode:

$$for\ holes: x_B = W_b - x_n \ll L_p \qquad (4)$$

$$for\ electrons: x_E = W_E - x_p \ll L_n \qquad (5)$$

Where L is called diffusion length and represents the average distance that a minority carrier travels before recombining. Considering for instance the hole current, this is therefore greatest at $x = x_n$, the edge of the space-charge region, and decreases away from the junction because the hole concentration gradient decreases as carriers are lost by recombination (analogous for electrons).

In this case, almost all the injected minority carriers recombine at the ohmic contacts at either ends of the diode structure and thus the excess minority carrier distribution can be approximated essentially in a linear way. In short base diode, I_s depends on $\frac{q\, n_i^2\, D}{N_D x}$ (where x is the width of the p- or n-type region in the short-base diode case). For devices of this work, x is the wafer thickness.

The devices used in the present analysis can be considered short base diode for high purity of silicon, so there is great lifetime τ, that is equivalent to previous assumption of no recombination.

The technology, developed by STMicroelectronics, exploits deep ion implantation through high energy boron ions to produce monolithic structures with two stages, a thin ΔE stage (~ 2 μm in thickness) and a *E* stage (~ 700 μm in thickness), in a single silicon wafer, allowing to realize detectors with a sensitive thickness of few micrometres and a negligible field funnelling effect.

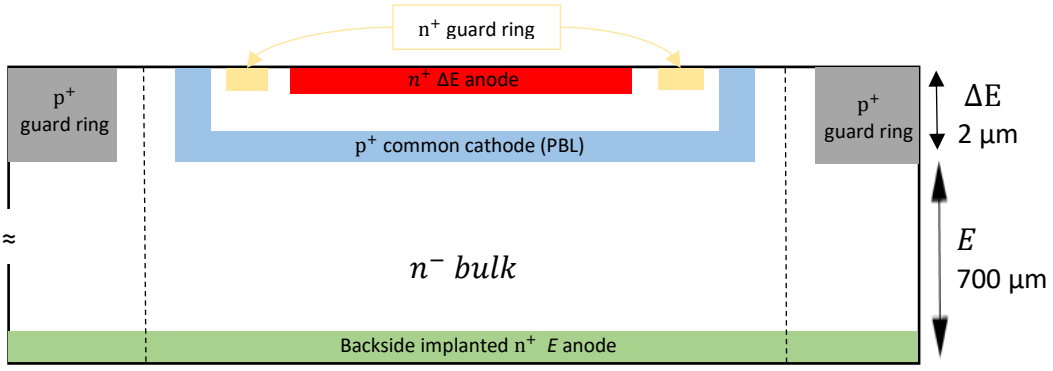

Fig. 3.3 - Schematic view of the detector used in the present project.

From the point of view of microdosimetric application, the ΔE stage provides micrometric size and E stage allows to recognise incident particles, therefore to make the correction for tissue equivalence. The ΔE anode (central blue region in Figure 3.4) is a superficial thin n-type layer obtained by depositing a 50 nm thick heavily doped polysilicon and by activating the dopant, P or As, with a thermal process.

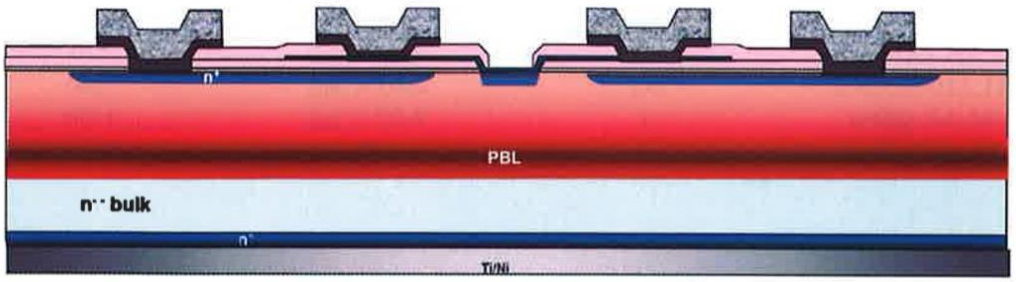

Fig. 3.4 – Cross section of the detector active area.

An n^+ ring is implanted around each ΔE cathode circle. This ring has the important function to avoid in the ΔE anode the collection of charge, coming from the edge of n-p junction. Therefore, the sensitive volume of the ΔE stage is sharply defined. A p^- well, obtained by implanting boron at very high energy (1 MeV) and by diffusing it, surrounds both the ΔE anode and the n^+ ring. With the boron implantation and the diffusion at the same time, the buried cathode and the p^- well are formed, as it's showed in Figure 3.4.

The buried cathode is common between the superficial and the bulk diode. A deep p^+ sunk region connects the common electrode to the superficial metal. The edge structure of the E stage is a p^+ ring surrounding completely the common cathode. This ring avoids the current injection across the lateral n-p junction and the flow inside the E diode. They are placed along all the bonding pads of the device above the thick oxide (1,2 μm). The anode of the E stage is the backside implanted n^+ layer. Laterally, an n^+ structure with a very large field plate is present as edge-of-die, as it's showed in

Figure 3.5. The charge collected in the E_{tot} stage, as in the present work, represents the sum of the charges released inside the ΔE stage and the E stage.

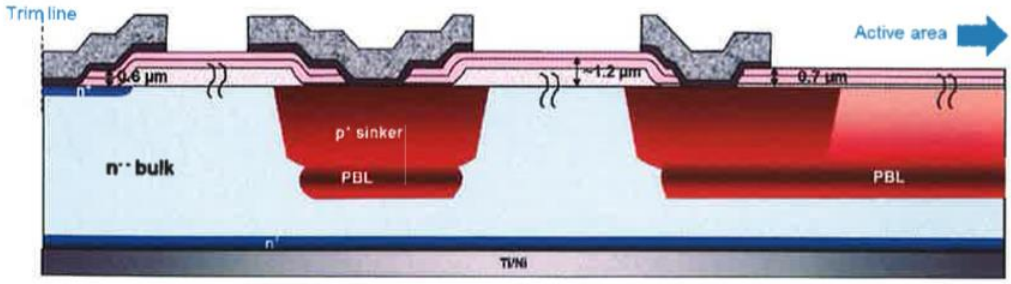

Fig. 3.5 – Cross section of the edge-of-die.

3.1 SLAB-0D-1 DEVICE

During the present thesis work the monolithic silicon telescope SLAB-0D-1 has been used for the longitudinal and transversal definition of the sensitive volume and for the damage study. The number of dimensions of the structure geometrical development (0D) and the ΔE area (1, in mm^2) are listed after the device name (SLAB).

The standard structure consists of a two stages detector, a ΔE stage and an E stage, about 2 and 700 µm in thickness, respectively. Its sensitive ΔE area is 1 mm^2 and the die size is 2.07 x 3.5 mm^2.

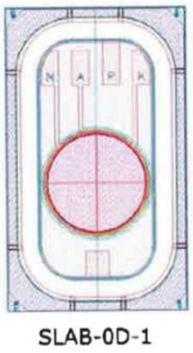

Fig. 3.6 – Layout of the detector used in the present project

3.2 SLAB-1D DEVICE

The definition of the longitudinal volume has been performed also for the SLAB-1D10/10-0.026 detector. It is one dimensional matrix of SLAB-OD detectors, so it has an independent E stage for each ΔE stage. The number before the slash gives information about the number of ΔE anodes (10), while the number after the slash indicates the number of cathodes (10). The number after the dash is the area expressed in mm^2 for each ΔE anode.

Therefore, each sensor has 10 ΔE anodes, 10 cathodes, one n^+ ring (surrounding all the anodes circles) and one very large p^+ ring (surrounding all the cathode rings), above which the metal buses and pads are placed. There are three pads useful to contact the p^+ ring. The anode E is accessible from the backside.

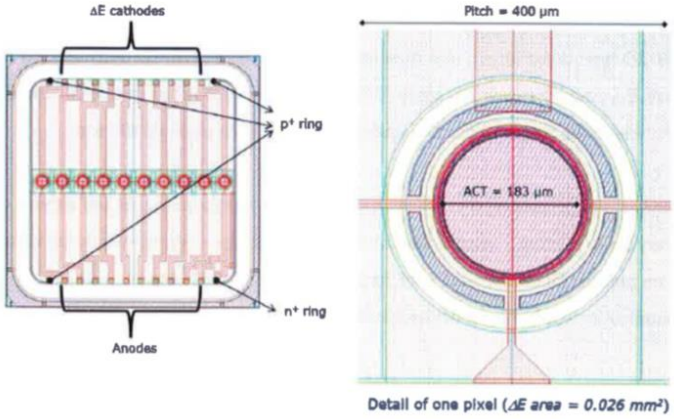

Figure 3.7 – Layout of the SLAB-1D10/10-0.026 detector and, on the right, a detail of one element.

3.4 MICRO-DISKS DEVICE

The hydrogen probe was used to investigate the border definition of the Micro-Disks (MD), a detector with one segmented ΔE stage and one large E stage.

There are several designs of these microdosimeters, with two variable geometrical parameters: the dimension of the pixel matrix and the pixel diameter. In the present work, the detector diameter is 2 µm, with 1 pixel and a sensor size of 1.53×1.79 µm^2. The code is MD-2, where the number before the dash indicates the number of pixel (1 when not written) and the number after the dash refers to the pixel diameter, expressed in µm. The ΔE/E ratio is 1:1.

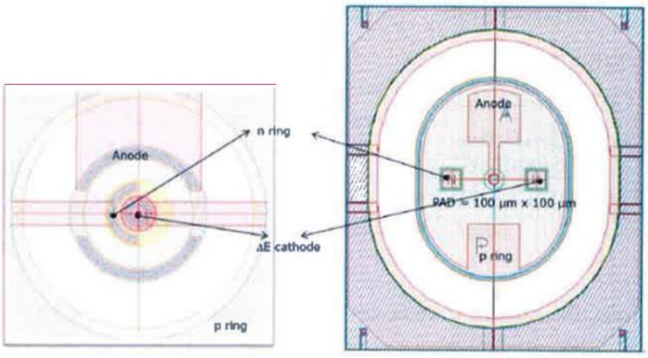

Figure 3.8 - Micro-disk with one element (MD-2).

3.3 RUĐER BOŠKOVIĆ INSTITUTE FACILITY AND EXPERIMENTAL SET-UP

The experimental part of this thesis work was performed in two separate shifts at Ruđer Bošković Institute in Zagreb. The first shift was at the end of January and the second one at the beginning of Febraury (2017), separated by eleven days.

The accelerator facility consists of two electrostatic tandem accelerators, the 1.0 MV HVEC ENTandem Van de Graaff and the 6.0 MV HVE Tandetron, as well as 8 beam lines. One of the beam lines can accept simultaneously ion beams from both accelerators. The following figure shows a schematic view of the laboratory.

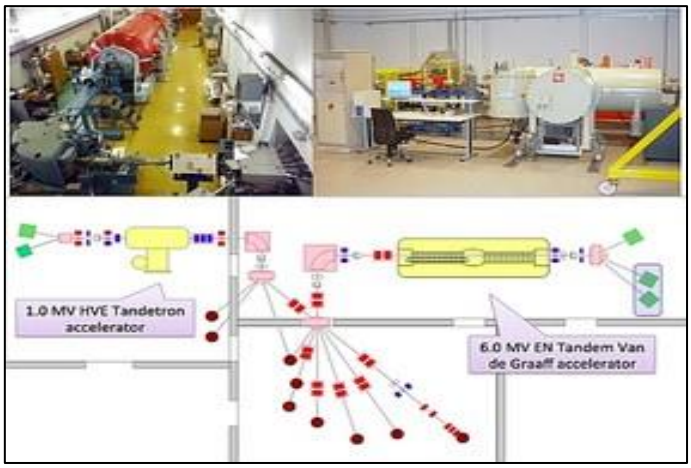

Figure 3.9 – View of the laboratory of Ruđer Bošković Institute (Zagreb) for ion beam interactions.

The EN Tandem Van de Graaff accelerator has three ion sources, namely RF source with charge exchange for He ions, a multi-cathode sputtering ion source for a variety of ion species (H, Li, B, C, O, Si, Cl, Cu, Br, Au, etc.) and finally a home built sputtering source for rare beams including short lived radioactive beams. For the presented experiments it was always used the EN Tandem Van de Graaf accelerator.

The Tandetron accelerator is equipped with a direct extraction duoplasmatron source (for negative hydrogen ions) and a sputtering ion source used for other ions (typically Li, C, O, Si, and heavier). Presently, there are nine available end stations.

Different particle beams were used to perform the experiments. Detailed informations about them are listed in the following table.

Particle	Mass [amu]	Charge	Energy [KeV]	Energy/nucleon [KeV]
Carbon	12	4	15000	1250
Silicon	28	3	3616	129.1454082
Lithium	7	3	14464	2066.326531
Proton	1,007	1	2000	1986.097319

Table 3.1 Description of the characteristics of the particles accelerated by the EN Tandem Van de Graaf at Ruđer Bošković Institute (Zagreb).

All the particles chosen completely stop inside the dimension of the E layer, so to give a signal directly related to the particle energy.
The detectors were adapted to a support placed inside the vacuum chamber, where the particle beam could irradiate them.

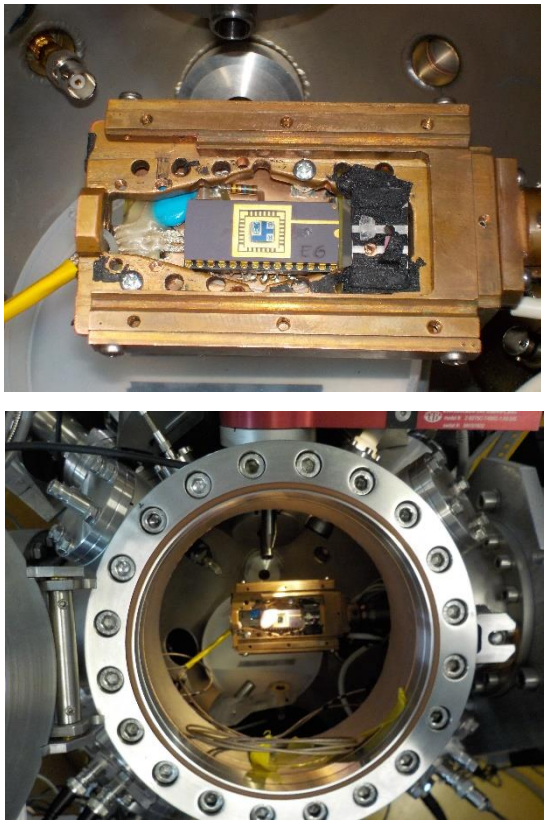

Figure 3.10 – View of the SLAB-0D-1 device fixed on the metallic substrate inside the vacuum chamber at Ruđer Bošković Institute (Zagreb).

The output signal enters in the first element of the electronical chain: a bi-channel spectroscopy amplifier named BICE 4. It's an aluminium box housing two spectroscopy channels. Its design offers low noise, stability, and its integrating nature provides an output proportional to the total charge flowing from the detector during the pulse event. During the experimental activities, different models of Cremat preamplifier have been used. Downstream this charge sensitive preamplifier, a shaping amplifier

produces a Gaussian-shaped pulse. Downstream of this stage the signal to noise ratio is considerably improved.

Therefore, at the input of the charge sensitive preamplifier the signal is a current pulse with Dirac's delta shape. Then, at the entrance of the amplifier, the signal looks like a voltage step. Finally, the amplifier gives back a Gaussian shaped signal. The signal was then collected with two different systems, one of the two is the calibrated system that will be used in all the present work to perform the calibration of the signals collected from the second system.

Chapter IV

LONGITUDINAL DEFINITION OF ACTIVE VOLUME

The purpose of the presented analysis is to estimate the thickness of the ΔE layer and of the dead layer of the silicon telescope. For a correct evaluation of the microdosimetric parameters, the precise sensitive thickness must be known. This evaluation was performed by analysing the detector response to different ion probes, carbon, silicon and lithium via the IBIC technique, as a function of the incidence angle between the beam direction and the normal to the detector surface. The scanned microbeam was used to perform a beam induced charge (IBIC) process, which consists in a repeated random scan of the area of interest to statistically ensure an irradiation of all the voxels with the same number of particles. This process is characterized by a low fluence rate (about $10^7\ ions \cdot cm^{-2} \cdot s$), in order to assess the dosimeter response in terms of charge transport properties at microscopic level with high spatial resolution.

4.1 SLAB-1D DEVICE

The detector SLAB-1D was tested with a 15 MeV carbon ion beam entering the detector surface at 0°, 30°, 45°, 60°, -30°. By assuming a constant stopping power uniformity of the particles crossing the first 2 μm of silicon detector (the average value is obtained from TRIM simulations, see Figure 4.1), at 0° and different incidence angles, it is possible to write a system of equations that links the energy loss inside a superficial

silicon equivalent dead layer (proportional to $1/\cos\alpha$, with α = incidence angle) and the signal acquired in the E_{tot} stage.

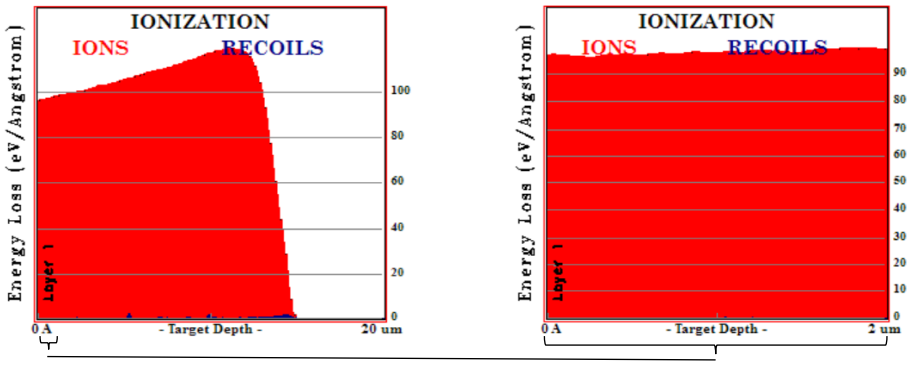

Fig. 4.1 – Stopping power of a 15 MeV carbon ions crossing a silicon detector with an angle of incidence of 0°. The figure on the right shows that the first 2 μm are inside the plateau and the ionizations are constant. (SRIM 2008)

The system for the incidence angles of 0°, 30°, 45°, 60° is the following:

$$\begin{cases} E - x = P_{mV}(o°) \cdot K \\ E - \dfrac{x}{\cos 30} = P_{mV}(30°) \cdot K \\ E - \dfrac{x}{\cos 45} = P_{mV}(45°) \cdot K \\ E - \dfrac{x}{\cos 60} = P_{mV}(60°) \cdot K \end{cases} \quad (1)$$

Where E is the particle energy (15 MeV in this case), x is the energy loss inside the dead layer in MeV, $P_{mV}(0°)$ is the signal amplitude in mV and K is the calibration coefficient from mV to MeV. The calibration of the E_{tot} stage signal amplitude is done indirectly by basing on the same data collected with a second calibrated electronic chain.

Being an overdetermined system of two unknowns and four equations, MATLAB software solves it through the method of least squares.

By applying the calibration coefficient K to the collected experimental data, an increase of energy loss inside the dead layer at increasing incidence angle can be observed, as well as inside the ΔE layer, due to the increased carbon ions path.

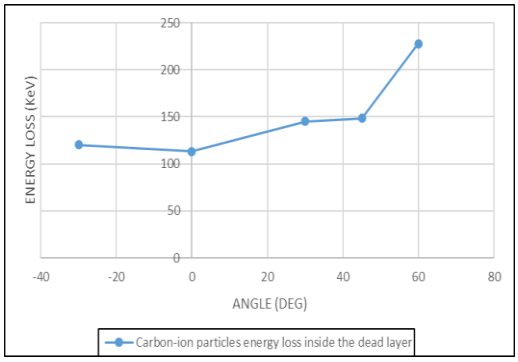

Figure 4.2 – Carbon-ion particles energy loss (KeV) inside the dead layer at different tilting angles (-30°, 0°, 30°, 45°, 60°), obtained by applying the conversion factor K from system (1).

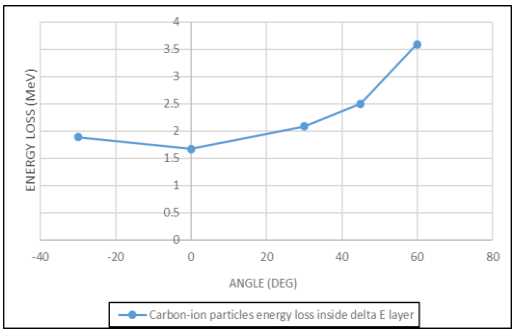

Figure 4.3 – Carbon-ion particles energy loss (MeV) inside the ΔE layer at different tilting angles (-30°, 0°, 30°, 45°, 60°), converting experimental data with the conversion factor previously obtained in the laboratory at Politecnico di Milano.

The asymmetry of the curves for values -30° and +30° is possibly due to the contribution of random errors linked to the low resolution of the measure and systematic errors in tilting procedure.

By relating the energy value at the detector entrance (15 MeV) with the estimated value of energy loss inside the dead layer in the case of an incidence angle of 0°, referring to SRIM tables, a dead layer of (0.120 $\pm$ 0.004) μm silicon equivalent was

found. A general SRIM uncertainty of 3.5 % on ranges of carbon, silicon and lithium ions in a silicon layer is adopted here [29].
Simply scaling for the relative density, it corresponds to (0.136 ± 0.005) μm silicon oxide (SiO_2).
In the same way, by considering the estimated energy value at the entrance of ΔE, i.e. the energy value at the detector entrance decreased of the energy loss inside the dead layer, and the energy lost in the same thin layer, the estimated ΔE thickness results to be (1.71 ± 0.06) μm.

4.2 SLAB-0D-1 DEVICE

The same method was applied to another type of detector. Unfortunately, in this case the pulse eight acquisition was affected by high systematic errors. We estimated those errors (see Appendix) and applied a correction to the pulse amplitude.

- **Assessment of the dead layer thickness**

Detector SLAB-0D-1 was irradiated with 15 MeV carbon ions, 3.616 MeV silicon ions and 14.464 MeV lithium ions, each one with different incidence angles.
The dead layer thickness was estimated with the same method described in the previous section. For carbon and lithium, the particles range in silicon is much higher than 2 μm, (around 15 μm for carbon and 43 μm for lithium) and, as we can see from the SRIM simulation (figure 4.4 and figure 4.5), the first 2 μm are inside the plateau region. Therefore, the electronic stopping power was assumed to be constant in this thin dead layer. However, it should be noticed that the energy released by lithium particles in the first part of their path is much lower than in the case of carbon ions. For lithium ions, the detector resolution does not allow to see some differences in the released energy at different incident angles and then the data collected in this case do not provide any useful information about the dead layer thickness.

For silicon ions, the situation is different because the detector is not placed in the plateau side, but in the distal part of the Bragg-peak (figure 4.4). Since the dead layer thickness is expected to be of the order of 100 nm, we can roughly assume that the stopping power is constant for all the angles and that the energy loss across the dead layer is proportional to the angle of incidence, as in the other cases.

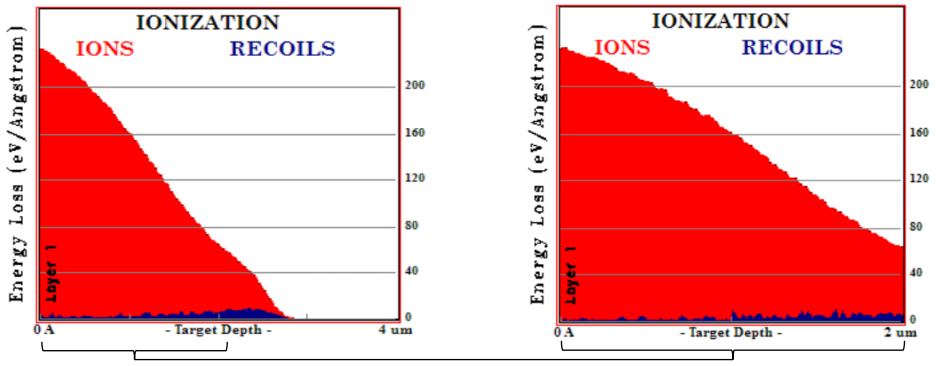

Fig. 4.4 – Stopping power of a 3.616 MeV silicon ions crossing a silicon detector with an angle of incidence of 0°. The figure shows that we aren't in the plateau side, but we are in the distal part of Bragg peak.

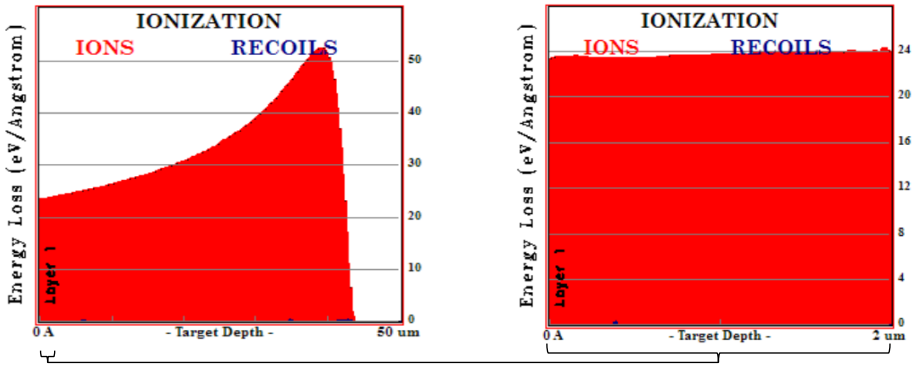

Fig. 4.5– Stopping power of a 14.464 MeV lithium ions crossing a silicon detector with an angle of incidence of 0°. The figure on the right shows that the first 2 μm are inside the plateau region.

Therefore, a system of equations similar to the one described in the previous section (system 1) was applied for carbon ions impinging the detector at 0°, 30°, 45°, 60°, and

for silicon ions at 0°, 30°, 45°, 50°, 55° and 60°. The energy calibration for the E_{tot} stage was performed basing on the same data collected by the second calibrated electronical chain. As expected, the results show an increasing of energy loss inside the dead layer with increasing angle.

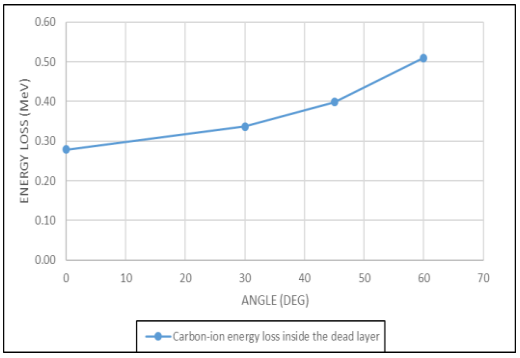

Fig. 4.6 – Carbon-ion particles energy loss (MeV) inside the dead layer at different tilting angles (0°, 30°, 45°, 60°), obtained by applying the conversion factor K from system (1).

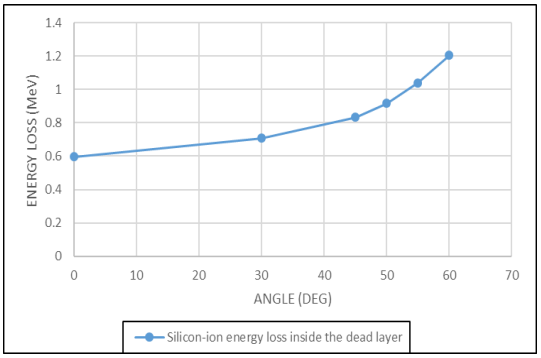

Fig. 4.7 – Silicon-ion particles energy loss (MeV) inside the dead layer at different tilting angles (0°, 30°, 45°, 50°, 55°, 60°), obtained by applying the conversion factor K from system (1).

By referring to SRIM stopping tables and by considering an uncertainty of 3.5 % [29], for detector SLAB-0D-1 the silicon equivalent dead layer thickness resulted to be (0.29 $\pm$ 0.01) µm and (0.26 $\pm$ 0.01) µm, for carbon and silicon probes, respectively. They correspond to (0.33 $\pm$ 0.01) µm and (0.30 $\pm$ 0.01) µm silicon oxide (SiO_2).

- **Assessment of ΔE thickness**

Spectrum of deposited energy in the ΔE stage showed the presence of a further unexpected peak at low energies, probably due to a charge induction in ΔE stage by E_{tot} stage.

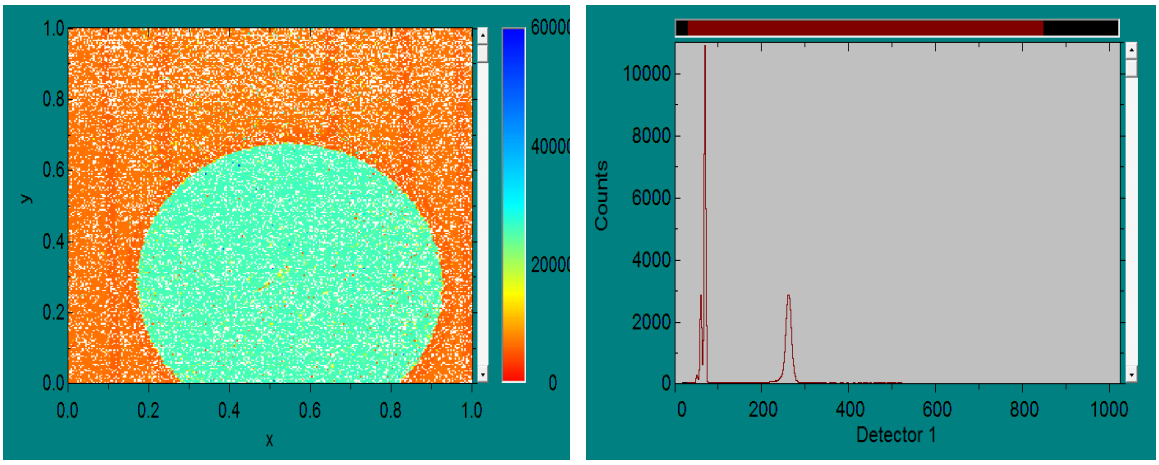

Fig. 4.8 – View of the sensitive area of the detector and the corresponding spectra (ΔE stage) for 15 MeV carbon ion beam entering the surface with 0°. It is evident the secondary peak at lower energy. (SPECTOR).

This further peak was fully subtracted from the primary signal by applying an iterative method and by optimizing the solution through the least square method in MATLAB [see Appendix for clarifications].

The amplitude-energy calibration for the ΔE stage was performed by exploiting the data acquired in the E_{tot} stage, because TRIM simulations showed that the range of 3.616 MeV silicon ions in silicon is less than 2 μm.

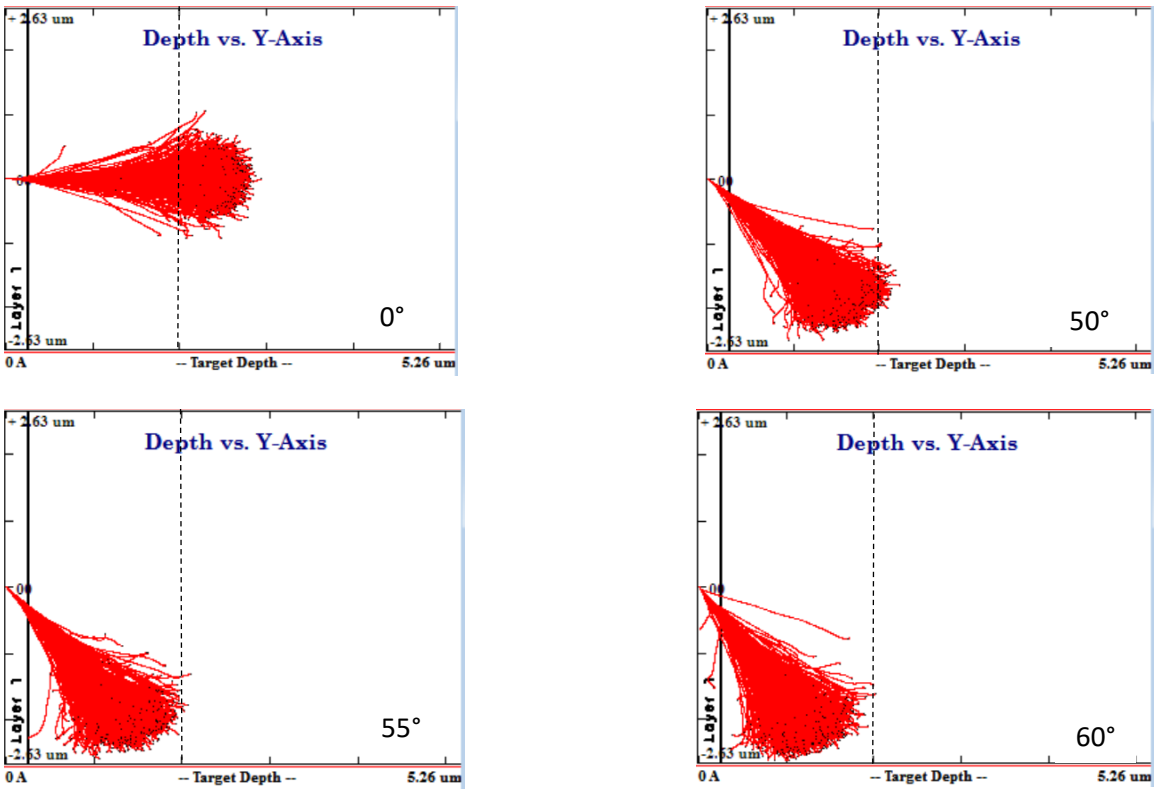

Fig. 4.9 – 3.616 MeV silicon-ion particles entering a silicon detector with increasing incidence angles from 0° to 60°, and crossing a silicon equivalent dead layer of 0.26 µm. As the angle increase, the travelled distance inside the detector thickness decrease. (TRIM 2008).

Under the hypothesis that the thickness of ΔE layer corresponds to the nominal value of 2 µm, we can assume that for the last three incidence angles (50°, 55°, 60°) the particles completely stop inside the thin ΔE layer and then the signals from ΔE and E_{tot} stages should be equal in energy, i.e.

$$E_{E_{tot},\alpha} = P_{\Delta E,\alpha} \cdot f \qquad (2)$$

Where α is the impinging angle (50°, 55°, 60°), $E_{E_{tot},\alpha}$ is the energy released in the E_{tot} stage in MeV by the silicon particles impinging the detector at α degrees, $P_{\Delta E,\alpha}$ is the signal amplitude of the ΔE stage in mV when the silicon beam crosses the detector at α degrees, and f is the calibration factor in MeV $\cdot$ mV^{-1}. The calibration factor f computed for silicon ions, is also hold for carbon and lithium ions.

For silicon and lithium ions, the energy at the entrance of the ΔE stage is equal to the beam energy (15 MeV for carbon and 3.616 MeV for silicon ions) decreased of the energy loss inside the dead layer, while the ΔE output energy is equal to the beam energy decreased of the energies released inside the ΔE stage and the dead layer. The entrance and output ΔE energies for carbon and lithium ions are then applied to SRIM range lookup tables to obtain the relative ΔE thickness.

Because of the very scattering situation, for low energy particles the use of the range lookup tables would be inappropriate. Then, for silicon particles, the ΔE thickness is computed basing on the Montecarlo simulation features of TRIM, which correlate the linear energy loss to the thickness.

Combining with MATLAB the results of the three ions, the ΔE thickness results to be (1.95 ± 0.08) μm [see Appendix].

Tables 4.1, 4.2, 4.3 show the comparison of the output energy of the ΔE stage simulated by TRIM with the output energy of the ΔE stage estimated with the presented method. The results are listed in the following table.

15 MeV CARBON	Evaluated output energy [keV]	TRIM simulation average energy [keV]	Difference %
0°	12727	12747	0.16%
30°	12465	12381	0.68%
45°	11774	11795	0.18%
60°	9949	10460	5.14%

Tab. 4.1 – Comparison between the energy values at the ΔE layer exit computed with the method explained in this section and obtained through TRIM simulations for 15 MeV carbon-ion beam. (TRIM 2008)

3.616 MeV SILICON	Evaluated output energy [keV]	TRIM simulation average energy [keV]	Difference %
0°	268	232	13.43%

Tab. 4.2 – Comparison between the energy values at the ΔE layer exit computed with the method explained in this section and obtained through TRIM simulations for 3.616 MeV silicon-ion beam. (TRIM 2008)

14.464 MeV LITHIUM	Predicted output energy [KeV]	TRIM simulation average energy [KeV]	Difference %
0°	13953	13975	0.16%
30°	14021	13892	0.92%
45°	13878	13785	0.67%
60°	13602	13474	0.94%

Tab. 4.3 – Comparison between the energy values at the ΔE layer exit computed with the method explained in this section and obtained through TRIM simulations for 14.464 MeV lithium-ion beam. (TRIM 2008)

The average difference between the two columns in the above tables is less than 1.11 %, except for silicon that shows a higher discrepancy. This discrepancy is due to the energy straggling affecting silicon ions in the proximity of the boundary between the ΔE and the E stages (fig. 4.8). Such a difference is acceptable, since the uncertainty of the data obtained through the least square method with MATLAB and the uncertainty related to the range lookup tables is about 4.50 %.

APPENDIX

As already mentioned, the spectrum of deposited energy in the ΔE stage showed the presence of a further unexpected peak at low energies. As an example, the following figure (Fig. 2) shows the spectrum of energy deposited in the ΔE stage by 15 MeV carbon ions at 0° incidence angle, where colour of each pixel in maps corresponds to the average signal height of all events that were recorded by the pixel.

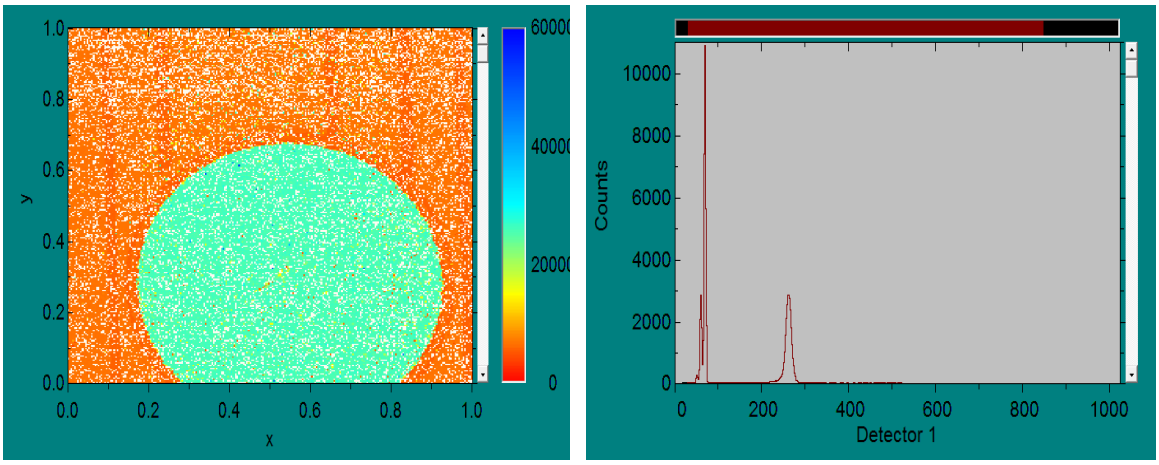

Figure 2 – View of the sensitive area of the detector and the corresponding spectra (ΔE stage) for 15 MeV carbon ion beam entering the surface with 0°. It is evident the secondary peak at lower energy. (SPECTOR).

It should be stressed that this further peak appears to depend linearly on the energy deposited in E_{tot} stage.

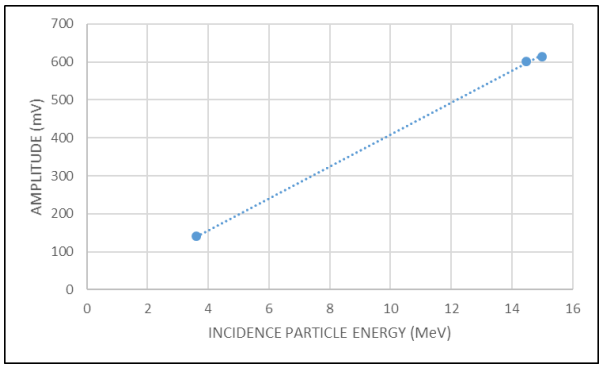

Figure 1 – Plot of the incidence particle energy (3.616 MeV, 14.464 MeV, 15 MeV) and the relative amplitude of the peak collected at lower energy. It's evident the proportionality between the two.

This unexpected signal should be due to a charge induction in ΔE stage by E_{tot} stage. The collected charge in E_{tot} stage is much higher with respect to the one collected in ΔE stage and it modifies the voltage on the common p^+ layer. Therefore, the voltage across ΔE stage varies by providing an injection of charge. The higher is the charge in E_{tot} stage, the higher is the injection in ΔE stage.

We assume that the second peak adds to the primary peak either entirely or partially. In other words, the primary peak is formed as follows:

$$P_{\Delta E} = P_{primary} + h \cdot P_{induced} \qquad (1)$$

$$P_{primary} = P_{\Delta E} - h \cdot P_{induced} \qquad (2)$$

Where $P_{\Delta E}$ represents the primary peak position, $P_{\substack{ionization \\ in\ \Delta E}}$ represents the peak position we are looking for, $P_{induced}$ represents the secondary peak position and h is the considered fraction ($h = ¼, ½, 1, 5/4$).

By referring to silicon ions, for every choice of h it was found the energy calibration factor to apply to the all the cases and the relative ΔE thicknesses (see Section 4.2).

As an example, for four different fraction of the peak position h, the results are listed in the following table.

Fraction of lower energy peak subtracted to the signal	ΔE thickness *Carbon*	*Silicon*	*Lithium*
$^1/_4$	2.51 µm	1.934 µm	4.07 µm
$^1/_2$	2.34 µm	1.938 µm	3.42 µm
1	2.02 µm	1.944 µm	2.08 µm
$^5/_4$	1.85 µm	1.947 µm	1.41 µm

Table 1 – Predicted ΔE thickness for three different ion probes and considering different fraction of lower subtracted peak to the signal. (SRIM 2008)

For each ion type, carbon, silicon and lithium, it was evaluated the dependence between the energy released in the ΔE stage and the considered value of *h*. The linear dependence found is showed in figure 2.

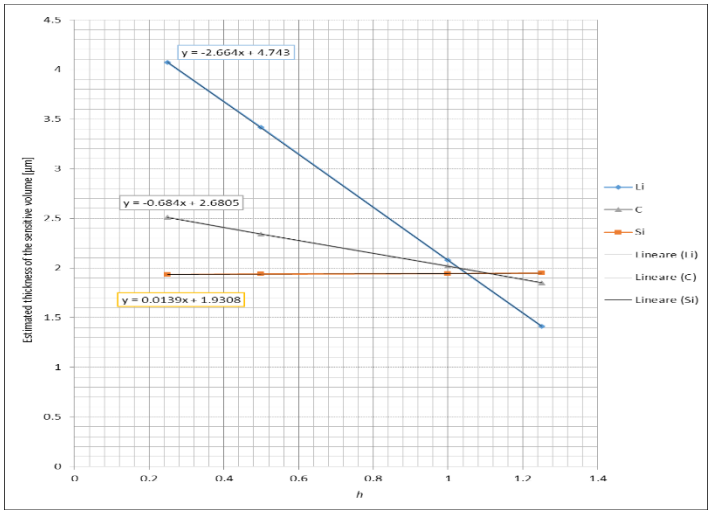

Figure 2 – Predicted ΔE thickness for three different ion probes and considering different fraction of lower subtracted peak to the signal. (SRIM 2008)

By assuming as the correct value of *h* the one that provides the same ΔE thicknesses in all the three cases, we optimized the intersection point of the three linear trends through the method of the least squares with MATLAB.

By considering the uncertainties of the method of the least squares with MATLAB software of about 0.69 % and of the SRIM stopping tables of about 3.5 % [29], the optimized solution is a subtraction of a peak fraction h equal to (1.05 ± 0.04), and the relative predicted ΔE layer thickness results (1.95 ± 0.08) μm.

Chapter V

TRANSVERSAL DEFINITION OF ACTIVE VOLUME

The purpose of this section is to estimate, by using microbeam scanning, the transversal size of the sensitive volume of detectors SLAB-0D-1 and MICRO-DISKS. A method is provided to define the size of the border profile, which represents the transition between the region providing a complete and homogeneous charge collection and the region where no charge is collected.

4.1 SLAB-0D-1 DEVICE

The sensitive volume of the detector is the region in which the energy deposition from ionizing particles is detected and its transversal size depends essentially on the shape of the electric field at the border. Ion Beam Induced Charge (IBIC) techniques evaluate pixel by pixel the average charge per ionizing particle. The size of the IBIC border profile is an overestimation of the border of the sensitive volume. In fact, the position of the ion probes used in the IBIC tests has an intrinsic uncertainty, which depends on the species and energies of the ion probes, and the beam focusing settings. Furthermore, the presence of secondary radiation, in particular δ-rays resulting in ionization around the primary particle trajectory, decreases the resolution of the method.

An irradiation with 15 MeV carbon-ion beam on detector SLAB-0D-1 was performed to investigate its border thickness. The absolute sizes of the IBIC maps were estimated by irradiating the detector covered with a calibrated 25 μm-pitch copper grid. The IBIC

scanning was repeated over the defined area of interest until all the pixels were irradiated. The maps show in each pixel the average charge produced per particle.
This process is characterized by a flux rate of about $10^7\ ions\ \cdot\ cm^{-2} \cdot s$ over square areas of the order of 100 µm × 100 µm.
The results of the IBIC test are shown in figure Fig 5.1, were the unit of the axis is the micrometers and the color scale is arbitrarily chosen to emphasize the areas with different response to irradiation. The central orange area on the left and the corresponding yellow-orange area on the right side represent the sensitive area of the detector for the stages E_{tot} and ΔE, respectively. The blue/green circle visible on the ΔE stage map (on the right) is the border we want to estimate.

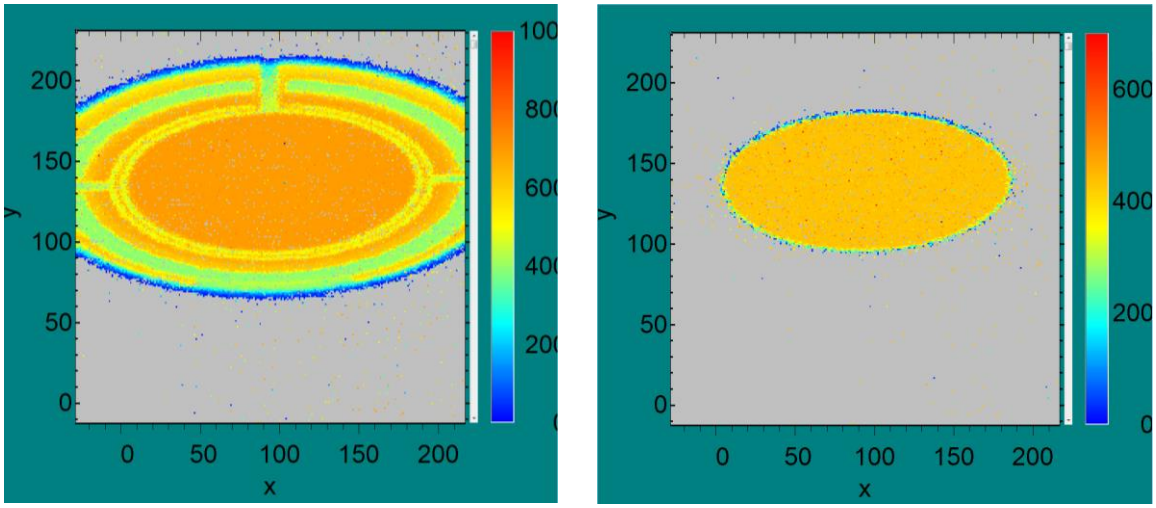

Fig. 5.1 – View of the SLAB-0D-1 E_{tot} layer (on the left) and ΔE layer (on the right) irradiated with 15 MeV carbon ions. (Spector software)

To better study the border we zoomed on the border region.

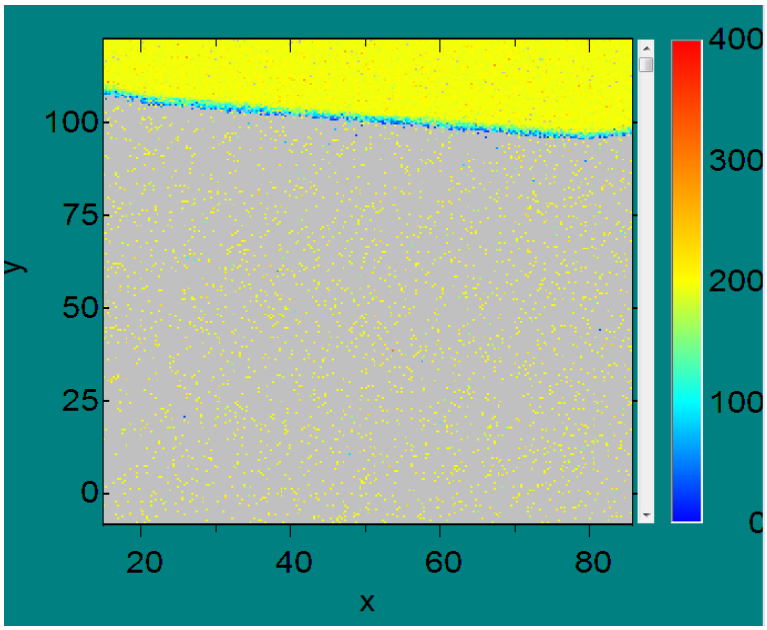

Fig. 5.2 – Focus on the SLAB-0D-1 border irradiated with 15 MeV carbon ions. (Spector software)

The yellow area corresponds to the sensitive area of the detector, the grey one is to the region outside the sensitive area and the border is represented with blue/green pixels. The presence of yellow dots in the grey area is due to the scattered ions that hit the sensitive area of the detector at random instants.

By selecting a line of pixel parallel to the y axis and by projecting it to the y axis, it is possible to obtain the profile shown in figure 5.3.

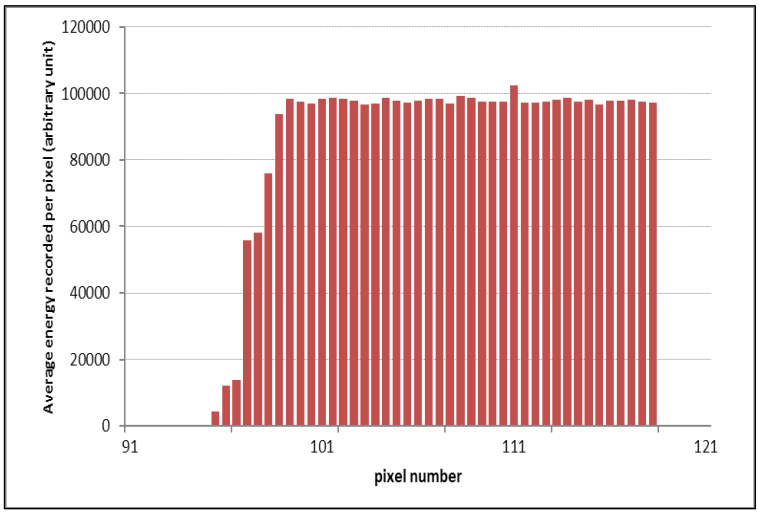

Fig. 5.3 – Projection to the y axis of a line of channels with identical x value. If a single pixel is hit by more than 1 particle the average energy value is reported.

In order to estimate the profile size, the data were interpolated with a sigmoid function, represented by the following expression:

$$S(x) = \frac{a}{1+e^{\frac{b-x}{c}}} \qquad (1)$$

The three parameters *a, b,* and *c* are correlated to the sigmoid upper asymptotic value, position of the inflection point, and steepness at the inflection point, respectively.

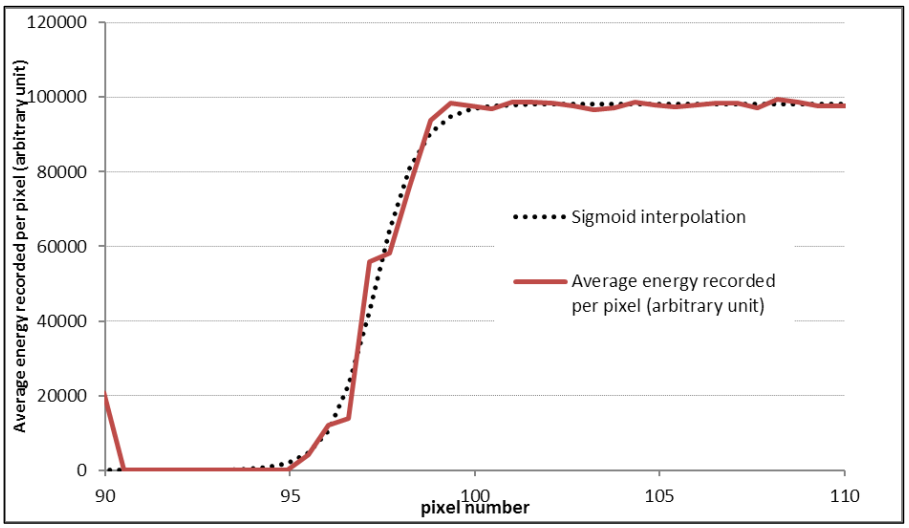

Figure 5.4 – Sigmoid interpolation of the experimental data.

An estimation of the size of the border is given by considering the function tangent to the sigmoid inflection point and then by determining the difference between the abscissa of its intersections with the horizontal asymptote and with the x axis. It is possible to demonstrate that this difference corresponds to $4 \cdot c$.

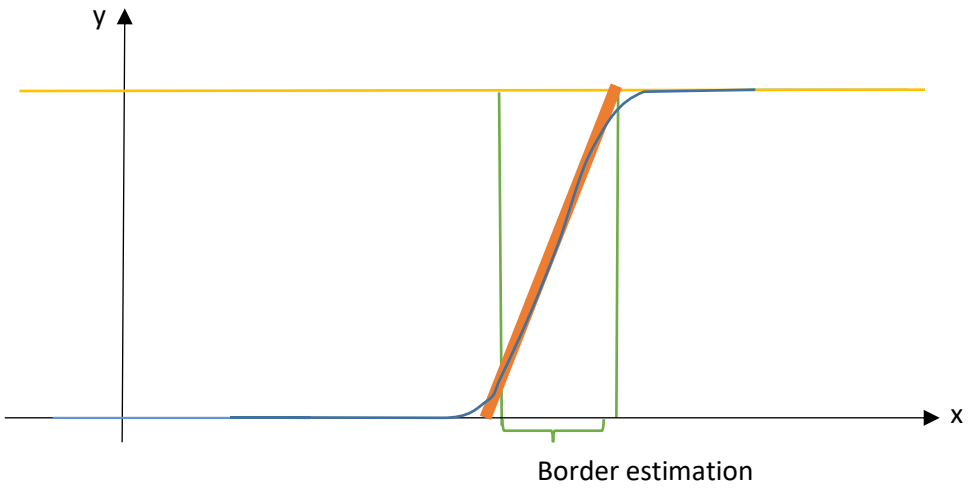

Figure 5.5 – Sigmoid function (blue line), tangent to the inflection point (orange line), horizontal asymptote (yellow line), distance between the abscissa of the tangent intersections with the horizontal asymptote and with the x axis (green line).

The interpolation between the experimental data and the sigmoid function provides a value of the parameter c and therefore an estimation of the border.
The evaluation of the border size was repeated for different lines of pixels parallel to the y axis. The average value of the parameter c resulted 0.83 µm, $\pm$ 0.18 µm, and consequently a value of the IBIC border thickness of 3.33 µm, $\pm$ 0.71 µm.

4.1 MICRO-DISKS DEVICE

The result of the IBIC analysis of the small detector Micro-Disks, by using 2 MeV hydrogen probe, is represented in fig 5.6. The magnification used in this analysis is 0.2. The axes are calibrated indirectly using a calibration performed with a calibrated 25 µm-pitch copper grid at magnification 0.5.

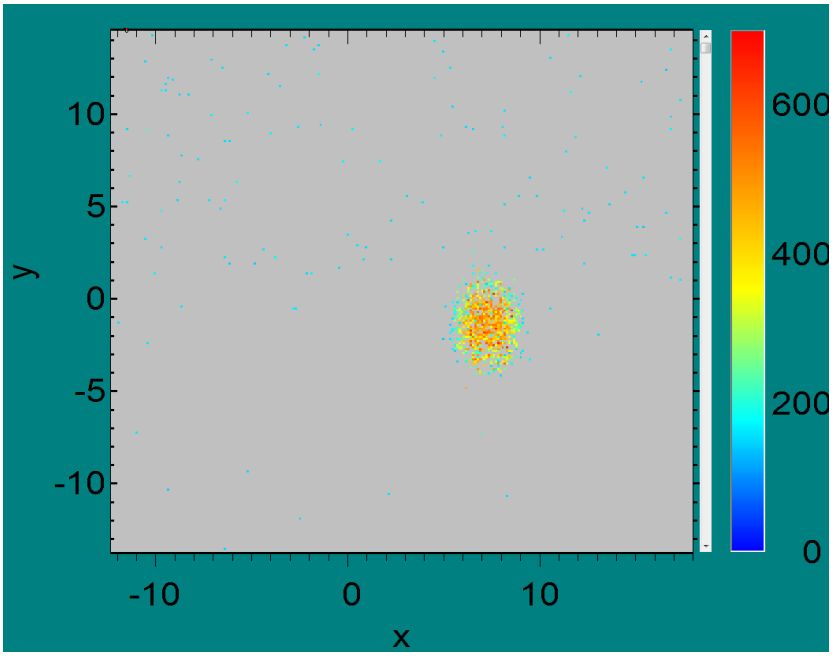

Figure 5.6 – View of the MICRO-DISKS and ΔE layer irradiated with 2 MeV protons. (Spector software)

Because of the small detector dimension, it is impossible to have a good statistics by collecting data just selecting random small region crossing the border, but we need to select a region including the entire device surface and project the results to the x and y axes in order to study the characteristics of the border.

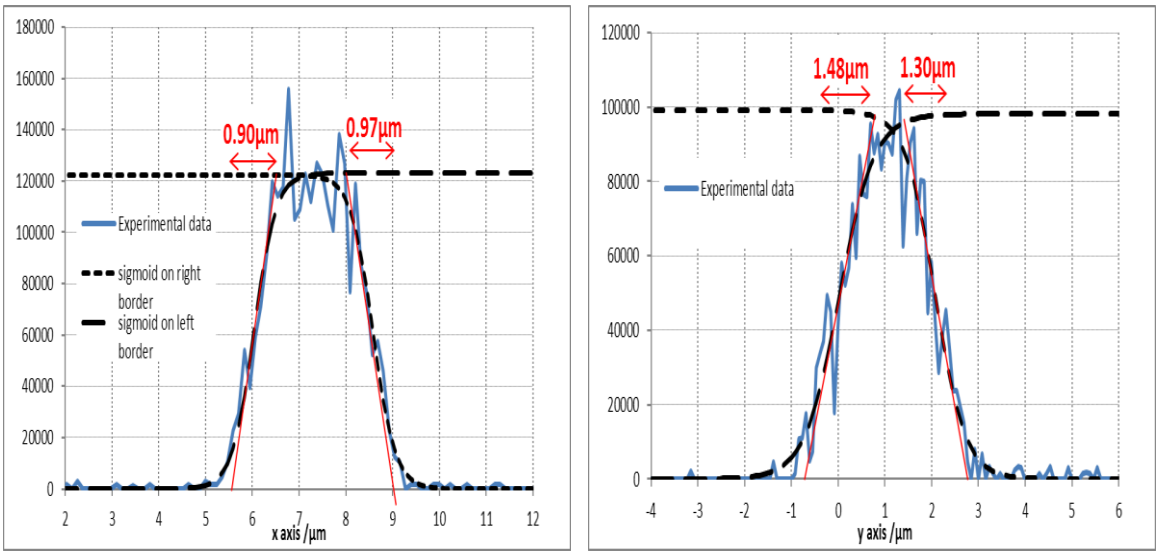

Figure 5.7 – Projection of the experimental data to the axes and sigmoid interpolation.

The interpolation of the experimental data on both sides with sigmoid functions was performed by following the procedure described in the previous section.

For the x axis, the estimated thickness of IBIC border results to be (0.90 $\pm$ 0.23) µm and (0.97 $\pm$ 0.24) µm for the left and the right side, respectively. For the y axis the estimated values of the border result for the left and right side to be (1.48 $\pm$ 0.37) µm and (1.30 $\pm$ 0.33) µm, respectively. The differences between the two axes values can be explained by considering the different resolution of the ion probe in the two directions (as it was reported by the Ruđer Bošković Institute [personal communication Natko Skukan Febrauary 2017]). A second element which

substantiates this observation is that for the y axis no flat region can be identified at the top. In contrast, for the x axis there is a flat region of the order of 1 μm.

The preliminary conclusion is that the border measurements are highly affected by the uncertainty of the ion probe. Due to the reduced size of the device it was impossible to repeat the evaluation of the border for different sets of pixels. The value of IBIC border assessed with these tests, is then 0.95 μm considering and uncertainty of 25 % which corresponds to $\pm$ 0.25 μm.

Chapter VI

RADIATION DAMAGE STUDY

Radiation hardness studies investigate the change in the detector SLAB-0D-1 properties after exposing it to a known amount of damaging particles, in the present work 3.616 MeV silicon ions and 15 MeV carbon ions. It is also presented a comparison between the performances of the same irradiated areas after 18 days, during which the detector has been maintained at room temperature.

6.1 RADIATION DAMAGE ANALYSIS

The radiation-induced damage test is performed using beams at high fluence rate (up to $3 \times 10^9\ ions\ \cdot cm^{-2}\ \cdot\ s^{-1}$), to deliver quasi-homogeneous number of particles over a defined cross area of the silicon sample. The quasi-homogeneity is assessed by scanning the beam several times over the sample, and therefore the particles, by arriving at random times, are randomly distributed over the surface. This procedure assures that all the pixels are irradiated. Under the hypothesis of no correlation between the times of arrival of the particles on the surface, we can assume that the number of particles for each pixel follow the Poisson distribution.

During this test, different ion fluence rates, 15 MeV carbon ions and 3.616 MeV silicon ions, were used to irradiate twelve small selective areas of 23.49 μm × 24.63 μm, each one at 46.98 μm (x axis) and 23.63 μm (y axis) in distance in the silicon case, and 176.16 μm (x axis) and 197.04 μm (y axis) in distance in the carbon case (see figure 6.1, referred to E_{tot} stage). The reference area represents the not damaged part of detector.

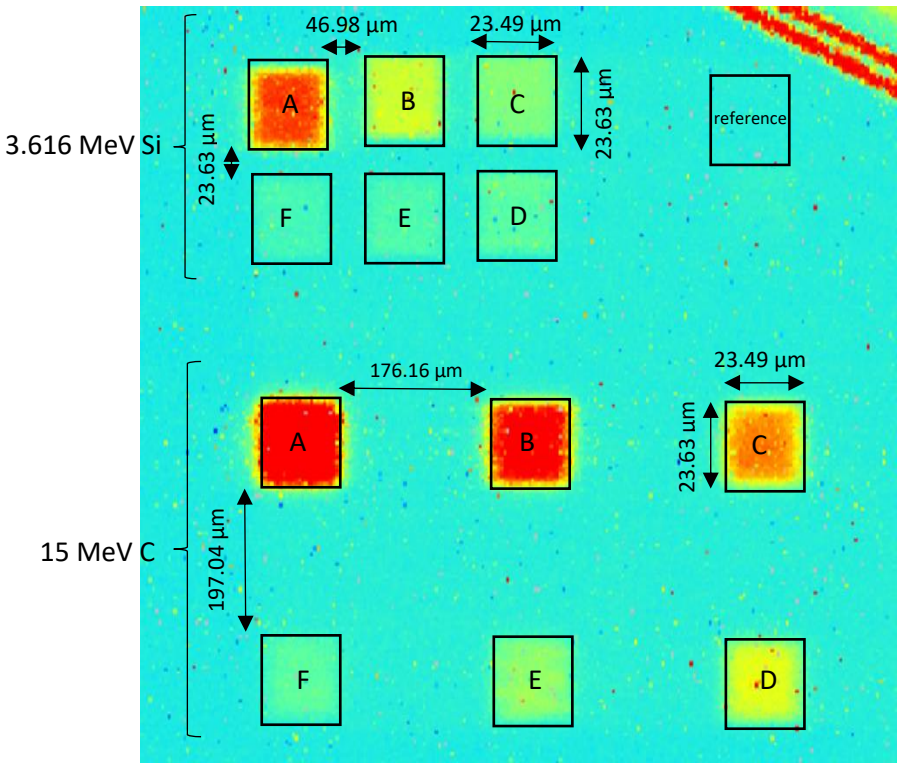

Fig. 6.1 – Schematic view of the irradiated areas of E_{tot} stage of the SLAB-01-D device.

The amount of impinging ions and the value of the calculated fluence for the different irradiated areas are reported in the following table.

CONSIDERED ION TYPE & AREA	IMPINGING IONS (#)	FLUENCE (IONS/μm^2)
15 MeV CARBON – A	1008000	1742.26
15 MeV CARBON – B	500000	864.22
15 MeV CARBON – C	253000	437.29
15 MeV CARBON – D	127000	219.51
15 MeV CARBON – E	63000	108.89
15 MeV CARBON – F	8000	13.83
3.616 MeV SILICON – A	1378000	2381.78
3.616 MeV SILICON – B	604000	1043.97
3.616 MeV SILICON – C	302000	521.99
3.616 MeV SILICON – D	163000	281.73
3.616 MeV SILICON – E	87500	151.24
3.616 MeV SILICON – F	75000	129.63

Tab. 6.1 – Fluence values of IBIC tests with 15 MeV carbon and 3.616 MeV silicon ions.

After irradiation that produces selectively damaged regions in the silicon detector, a beam induced charge (IBIC) analysis with 15 MeV carbon ions probe has been performed to measure the degradation of the charge collection efficiency. The results of ΔE and E_{tot} stages are shown in the following figure (fig. 6.2), where the unit of the axis is μm (to estimate the absolute size, a calibration is performed using a calibrated 25 μm-pitch copper grid) and the colour scale was arbitrarily chosen to point out the differences between the twelve irradiated areas. The blue zones represent the more damaged parts, which correspond to the lower charge collection efficiency.

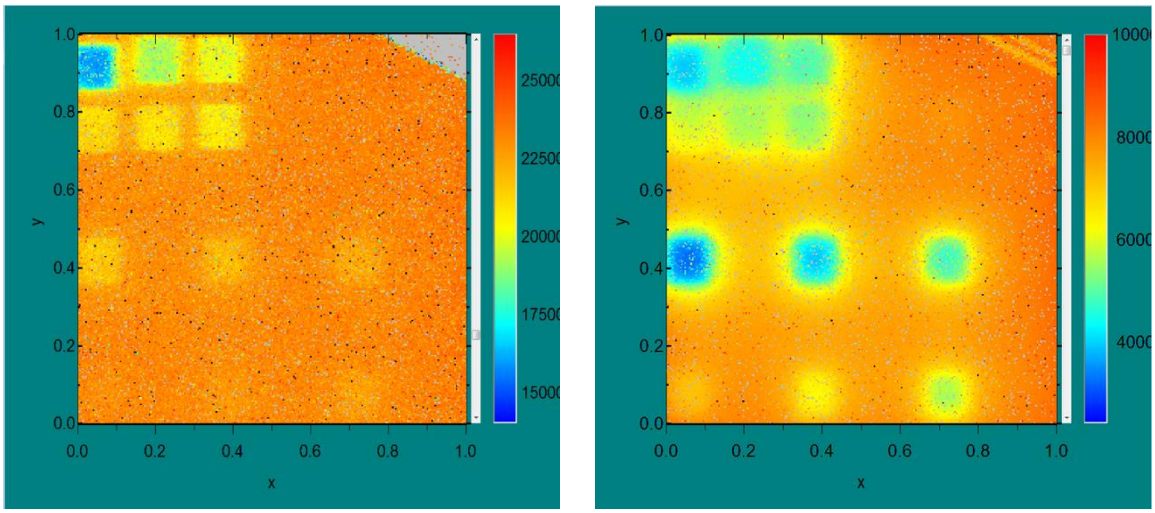

Fig. 6.2 – IBIC scan performed with 15 MeV carbon ions showing the irradiated areas with 15 MeV carbon ions and 3.616 MeV silicon ions. ΔE stage on the right side, E_{tot} stage on the left side. (20/01/2017, SPECTOR software).

After 18 days, the same IBIC test was performed and the twelve areas on a different colour scale are visible in the following figure. Since the detector was set on the support rotated of 180° respect to the first time we performed the irradiation, figure 6.3 appears rotated respect to figure 6.2.

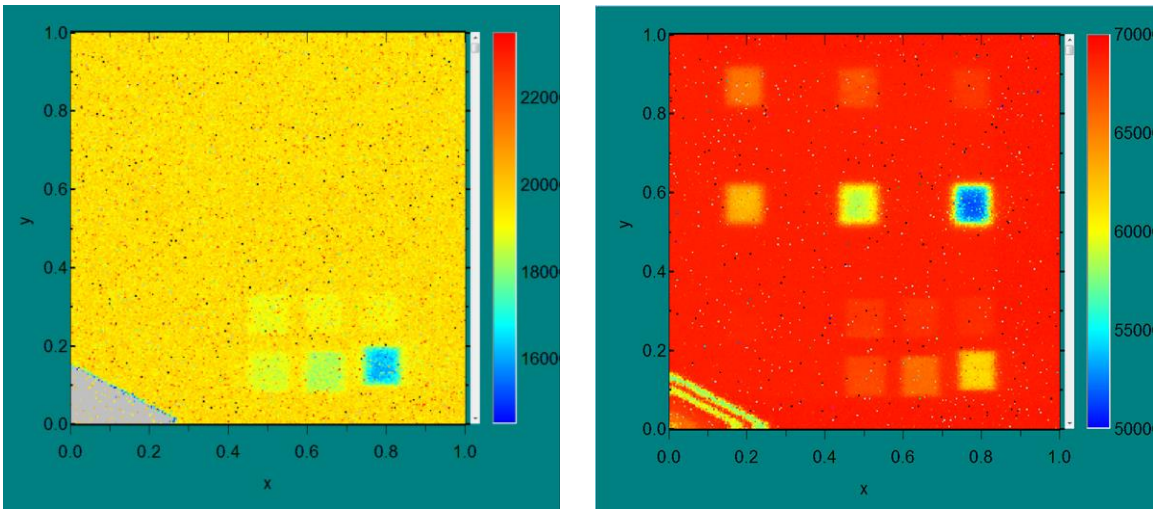

Fig. 6.3 – IBIC scan performed with 15 MeV carbon ions showing the irradiated areas with 15 MeV carbon ions and 3.616 MeV silicon ions. ΔE stage on the right side, E_{tot} stage on the left side. The image is rotated of 180° respect to figure 6.2. (08/02/2017, SPECTOR software)

The data were extracted from the damaged areas by selecting regions where the probability to have the same number of impinging particles is uniform.

The data of the first shift were corrected by subtracting the secondary peak (see chapter IV and Appendix for explanation) and the pulse-amplitude calibration was based on a comparison of data collected in parallel from another calibrated electronic chain (see chapter IV).

- **15 MeV carbon ion beam, ΔE stage**

The spectra of ΔE stage are shown in figure 6.4 for 15 MeV carbon ion beam.

Because different electronical chains were used during the two shifts of measurements, in the zoom boxes the *x* axes has been translated to have the reference peak, which represents the uniform region not damaged, visually in the same position and to better appreciate the differences in the peaks distance. For an easy understanding of the figure, just five selected regions of interest are reported.

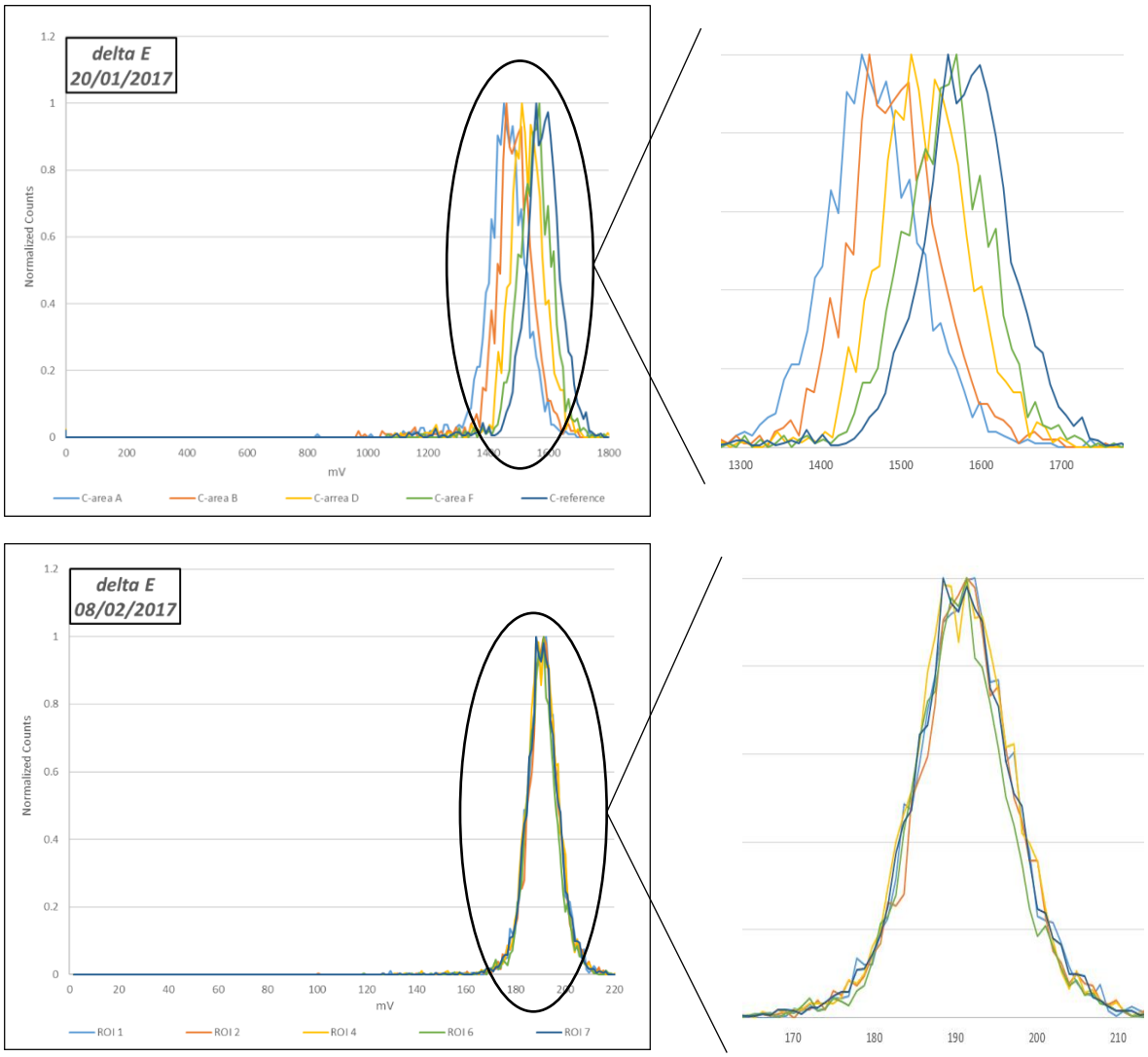

Fig. 6.4 – 15 MeV carbon ions normalized spectra relative to five selective areas measured at 18 days of distance for ΔE stage. In the zoom boxes the x axes has been translated to have the reference peak, which represents the uniform region not damaged, visually in the same position.

All the peak positions, extracted from the IBIC measurements, were computed through a Gaussian interpolation with MATLAB. The relative distance of all the peaks representing the damaged areas with respect to the position of the reference peak, just after the damaging irradiation and after 18 days, is reported in table 6.3 for 15 MeV carbon ions referred to ΔE stage.

CARBON FLUENCE (IONS/μm^2)	PEAK AMPLITUDE IN ΔE mV		RELATIVE DIFFERENCE %	
	20/01	08/02	20/01	08/02
AREA A - 1742.26	1463	190.70	-7.52	-0.05
AREA B - 864.22	1489	191.10	-5.88	0.16
AREA C - 437.29	1514	191.20	-4.29	0.21
AREA D - 219.51	1528	190.80	-3.41	-0.0
AREA E - 108.89	1544	190.20	-2.40	-0.31
AREA F - 19.36	1557	189.10	-1.58	-0.89
REFERENCE	1582	190.80		

Tab. 6.3 – Amplitude of the peaks of Figure 6.3 computed with a Gaussian interpolation (MATLAB) and the relative difference to the reference peak amplitude obtained in the pristine area. The relative differences express the difference between the reference peak amplitude and the peak amplitude of each area.

Figure 6.4 shows the effect of the radiation damage for all the irradiated areas as a function of the particle fluence and of the average dose, for 15 MeV carbon ions and ΔE stage.

The data of the peak amplitude are also provided as a function of the accumulated dose, obtained as the ratio of the total energy released in each area by the mass of the volumes, defined by the areas and the thickness of the ΔE stage.

By assuming a Gaussian distribution of the data collected for each area, the error bars consider the relative uncertainty on the measure and are equal to the average normalized standard deviation of the seven data-set collected for ΔE stage in each shift of measurement. For data collected on the first shift of measurement the uncertainty is around 5.02 %, while for the second shift it is around 3.31 %. Since data collected in the two different shifts are not correlated, the uncertainty of the difference is, according to the propagation of uncertainty, 6.01 %.

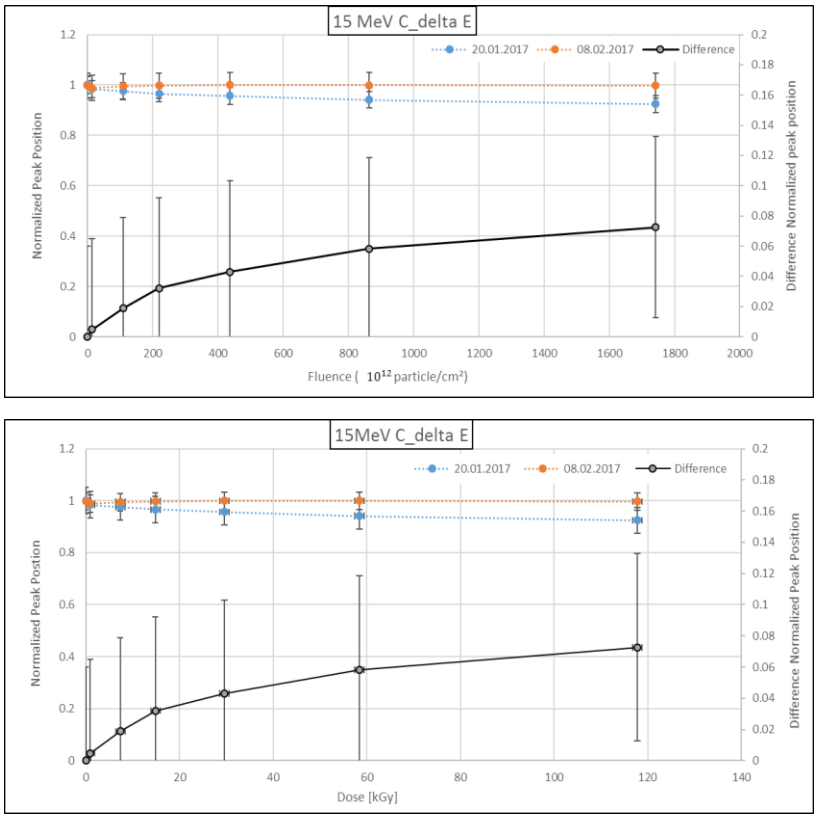

Fig. 6.4 – Normalized charge collection efficiency as a function of the fluence and as a function of the average absorbed dose for the ΔE layer for 15 MeV carbon ions at 18 days of distance.

- **15 MeV carbon ion beam, E_{tot} stage**

The spectra of E_{tot} stage are shown in figure 6.5 for 15 MeV carbon ions and E_{tot} stage. The zoom of the two figures in the boxes represents the x axes translated to have the reference peak visually in the same position and to better appreciate the differences in the peaks distance.

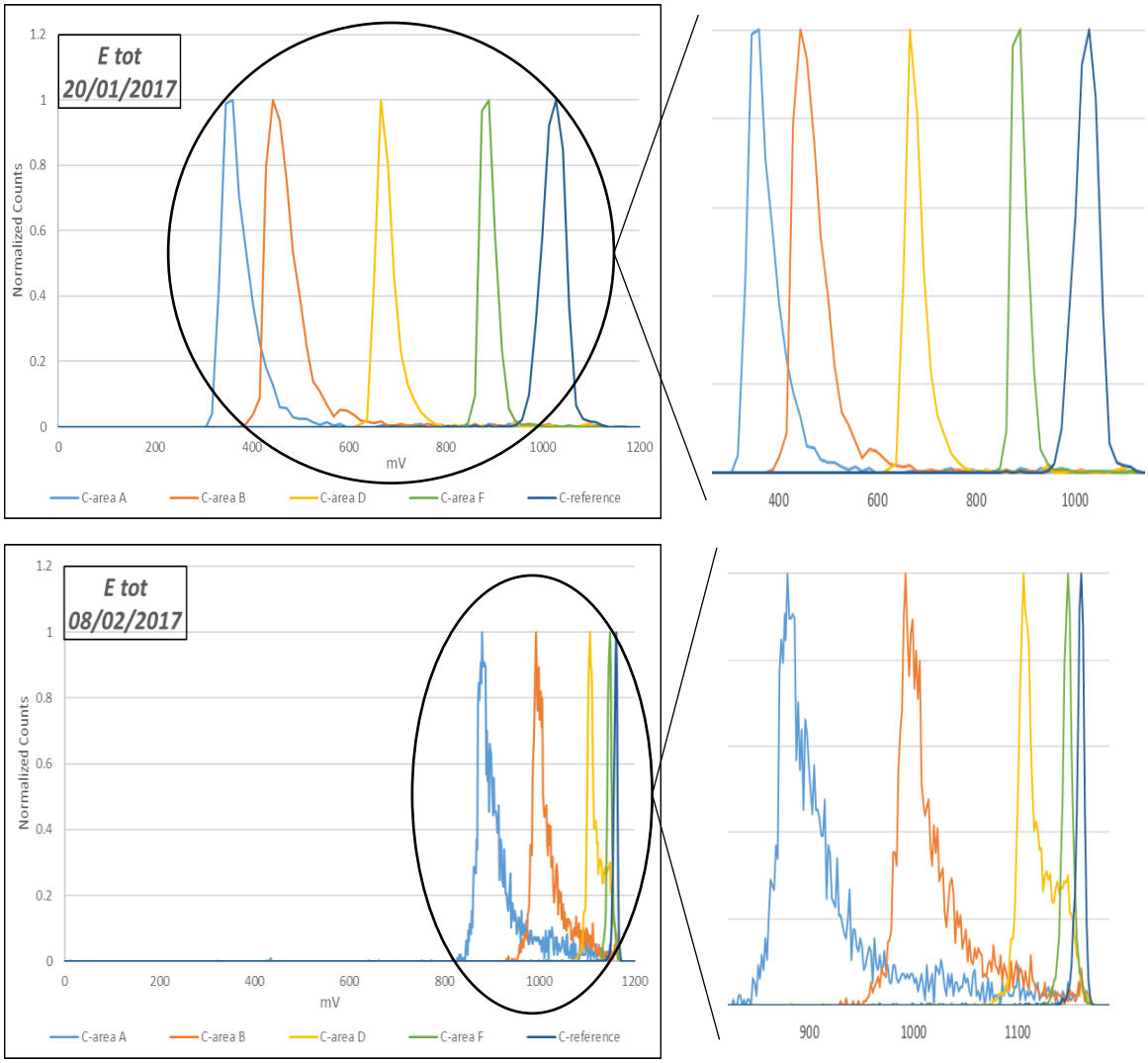

Fig. 6.5 – 15 MeV carbon ions normalized spectra relative to five selective areas measured at 18 days of distance for E_{tot} stage. In the zoom boxes the x axes has been translated to have the reference peak, which represents the uniform region not damaged, visually in the same position.

The relative distance of all the peaks representing the damaged areas respect to the position of the reference peak, just after the damaging irradiation and after 18 days, is reported in table 6.4 for 15 MeV carbon ions referred to E_{tot} stage.

CARBON FLUENCE (IONS/μm^2)	PEAK AMPLITUDE IN ΔE mV		RELATIVE DIFFERENCE %	
	20/01	08/02	20/01	08/02
AREA A - 1742.26	455.00	878.70	-55.57	-23.72
AREA B - 864.22	456.60	990.30	-55.41	-14.04
AREA C - 437.29	568.90	1057.00	-44.44	-8.25
AREA D - 219.51	672.90	1100.00	-34.28	-4.51
AREA E - 108.89	771.10	1123.00	-24.70	-2.52
AREA F - 19.36	885.90	1139.00	-13.48	-1.13
REFERENCE	1024	1152		

Tab. 6.4 – Amplitude of the peaks of Figure 6.5 computed with a Gaussian interpolation (MATLAB) and the relative difference to the reference peak amplitude obtained in the pristine area. The relative differences express the difference between the reference peak amplitude and the peak amplitude of each area.

Figure 6.6 shows the effect of the radiation damage for all the irradiated areas as a function of the particle fluence, for 15 MeV carbon ions and E_{tot} stage. For E_{tot} stage no correlation to the dose is provided. As in the previous case, by considering a Gaussian distribution of data, the error bars represented by the average standard deviation of the data collected for E_{tot} stage provide an uncertainty of around 5.02 % for the first data-set collected and around 1.26 % for the second one. The uncertainty on the difference is around 5.18 %.

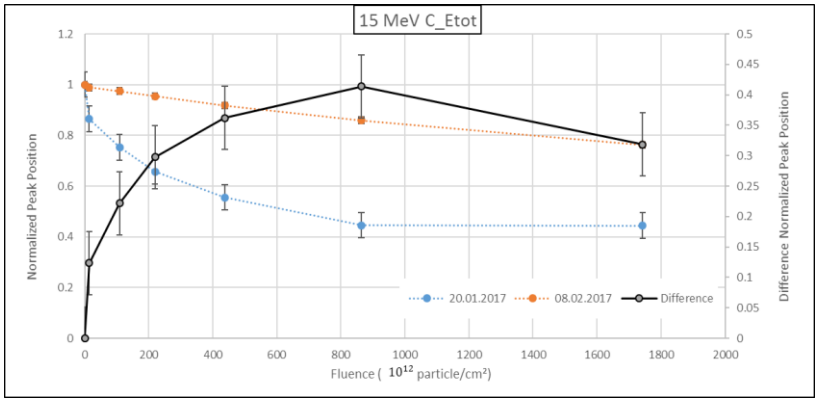

Fig. 6.6 – Normalized charge collection efficiency as a function of the fluence (a and c) and as a function of the total absorbed dose for the ΔE layer (b) for 15 MeV carbon ions at 18 days of distance.

- **3.616 MeV silicon ion beam, ΔE stage**

The spectra of ΔE stage are shown in figure 6.6 for 3.616 MeV silicon ions and E_{tot} stage.

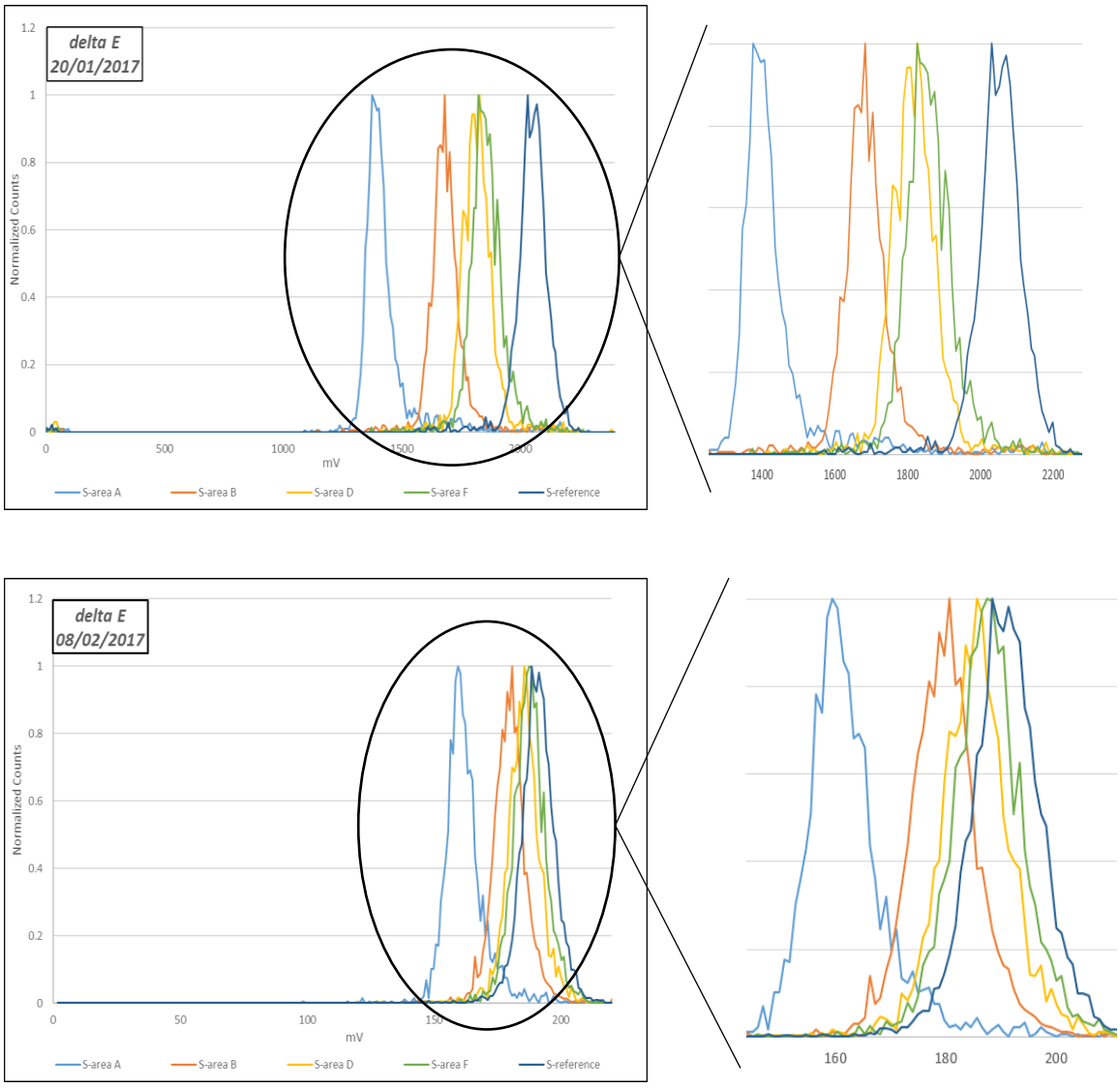

Fig. 6.7 – 3.616 MeV silicon ions normalized spectra relative to five selective areas measured at 18 days of distance for ΔE stage. In the zoom boxes the x axes has been translated to have the reference peak, which represents the uniform region not damaged, visually in the same position.

The relative distance of all the peaks with respect to the position of the reference peak, just after the damaging irradiation and after 18 days, is reported in table 6.5 for 3.616 MeV silicon ions and ΔE stage.

SILICON FLUENCE (IONS/μm^2)	PEAK AMPLITUDE IN ΔE mV		RELATIVE DIFFERENCE %	
	20/01	08/02	20/01	08/02
AREA A - 2381.781	1395	160.5	-32.11	-15.84
AREA B - 1043.974	1680	179.3	-18.25	-5.98
AREA C - 521.99	1761	182.50	-14.31	-4.30
AREA D - 281.7346	1815	185	-11.68	-2.99
AREA E - 151.24	1838	186.2	-10.56	-2.36
AREA F - 129.6325	1852	187.3	-9.88	-1.78
REFERENCE	2055	190.7		

Tab. 6.5 – Amplitude of the peaks of Figure 6.7 computed with a Gaussian interpolation (MATLAB) and the relative difference to the reference peak amplitude obtained in the pristine area. The relative differences express the difference between the reference peak amplitude and the peak amplitude of each area.

Figure 6.8 shows the effect of the radiation damage for all the irradiated areas as a function of the particle fluence and of the dose, for 3.616 MeV silicon ions and ΔE stage. By assuming a Gaussian distribution of data, the error bars, represented by the average standard deviation of data collected for ΔE stage, provide an uncertainty of around 3.72 % for the first data-set collected and around 3.63 % for the second one. The uncertainty of the difference is around 5.20 %.

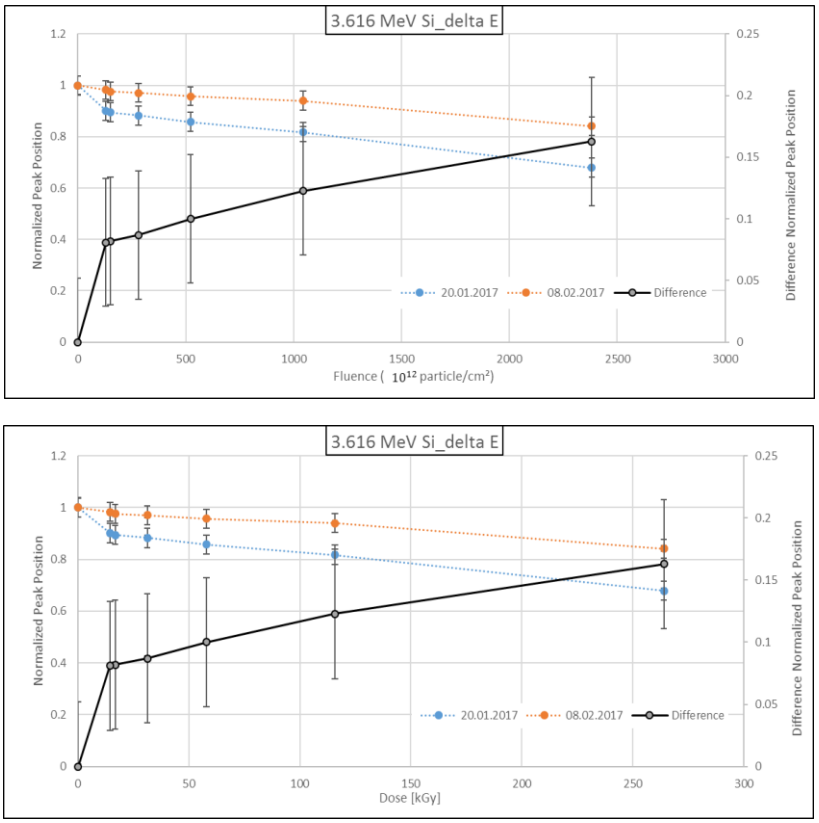

Fig. 6.8 – Normalized charge collection efficiency as a function of the fluence and as a function of the average absorbed dose for the ΔE layer for 3.616 MeV silicon ions at 18 days of distance.

- **3.616 MeV silicon ion beam, E_{tot} stage**

The spectra of E_{tot} stage are shown in figure 6.8 for 3.616 MeV silicon ion beam and E_{tot} stage.

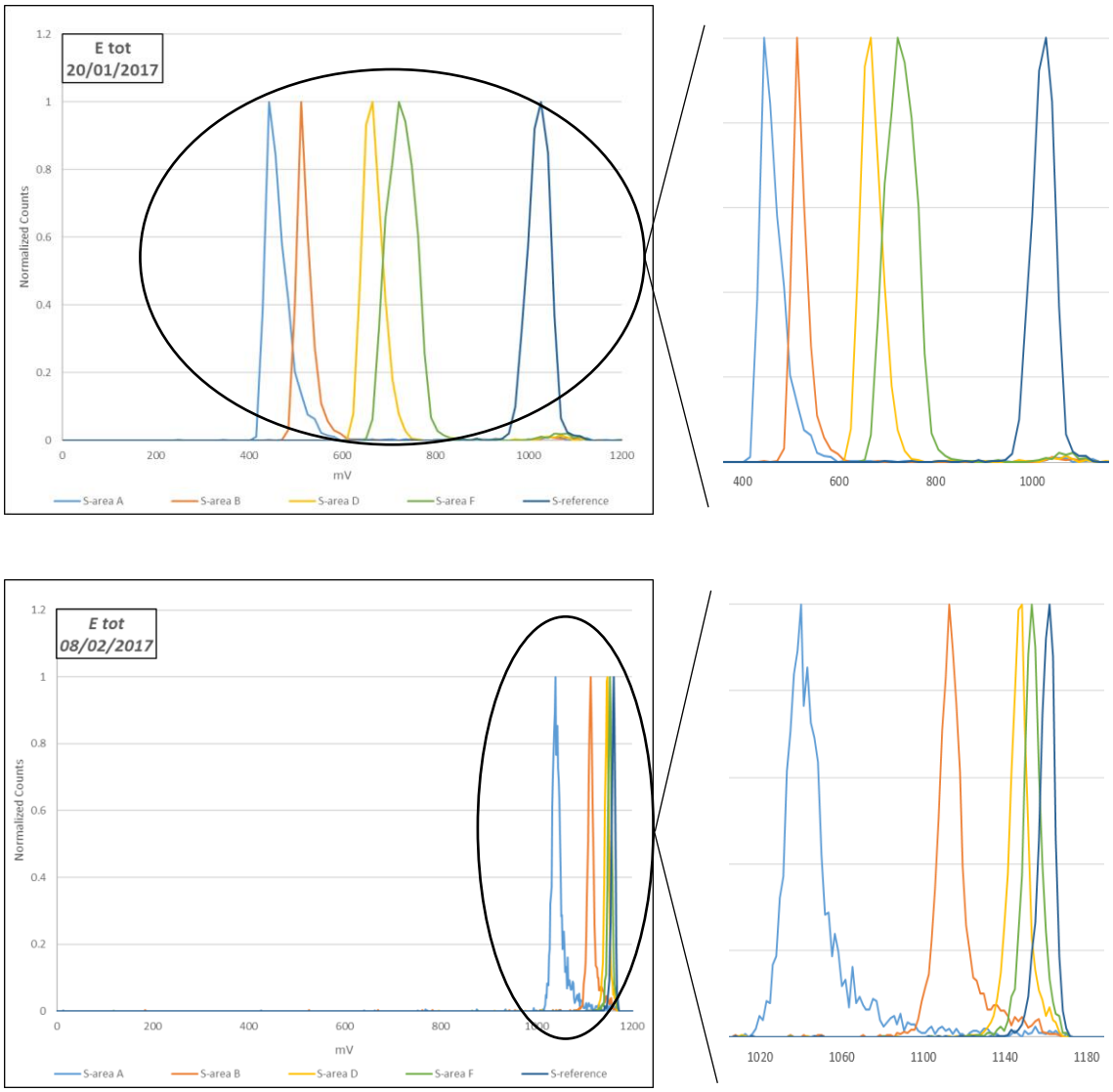

Fig. 6.8 – 3.616 MeV silcion ions normalized spectra relative to five selective areas measured at 18 days of distance for E_{tot} stage. In the zoom boxes the x axes has been translated to have the reference peak, which represents the uniform region not damaged, visually in the same position.

The relative distance of the all the peaks respect to the position of the reference peak, just after the damaging irradiation and at 18 days of distance, is reported in table 6.5 for 3.616 MeV silicon ions and E_{tot} stage.

SILICON FLUENCE (IONS/μm^2)	PEAK AMPLITUDE IN E_{tot} mV		RELATIVE DIFFERENCE %	
	20/01	08/02	20/01	08/02
2381.781	454.80	1041.00	-55.57	-10.34
1043.974	516.10	1113.00	-49.59	-4.13
	589.70	1113.00	-94.24	-4.13
281.7346	664.40	1147.00	-35.12	-1.20
	680.50	1150.00	-33.54	-4.13
129.6325	727.50	1153.00	-28.96	-0.69
REFERENCE	1024	1161.00		

Tab. 6.6 – Amplitude of the peaks of Figure 6.8 computed with a Gaussian interpolation (MATLAB) and the relative difference to the reference peak amplitude obtained in the pristine area. The relative differences express the difference between the reference peak amplitude and the peak amplitude of each area.

Figure 6.9 shows the effect of the radiation damage for all the irradiated areas as a function of the particle fluence, for 3.616 MeV silicon ions and E_{tot} stage. For E_{tot} stage no correlation to the dose is provided. The error bars, represented by the average standard deviation of data collected for E_{tot} stage, provide an uncertainty of around 4.31 % for the first data-set collected and around 0.61 % for the second one. The uncertainty on the difference is around 4.35 %.

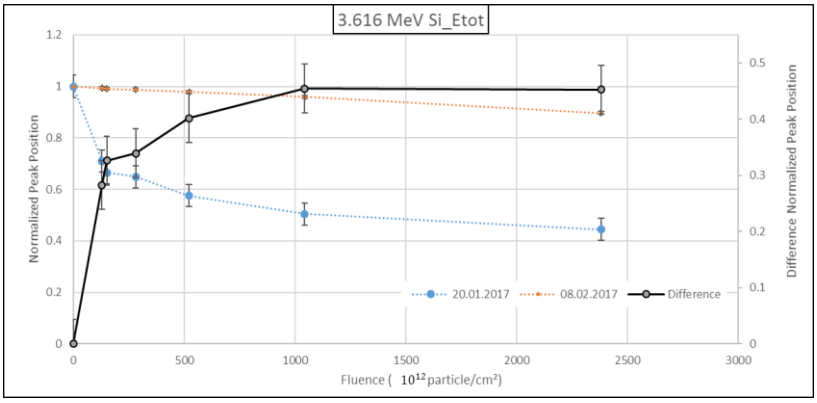

Fig. 6.9 – Normalized charge collection efficiency as a function of the fluence for the ΔE layer for 3.616 MeV silicon ions at 18 days of distance.

A time variation of the detector pulse amplitude was observed in these damaging irradiations. In all the cases described above, the IBIC tests performed immediately after the damage show a non-linear response: a drastic decrease of charge collection efficiency after the less intense damaging (both F areas of Fig. 6.1), followed by a less pronounced dependence at higher fluences.

Long term recovering phenomena are evident after 18 days from the irradiation, bringing back the detector performances towards the amplitude value shown on the pristine area, both for ΔE stage and E_{tot} stage and both for silicon and carbon case.

The interpolation of the curves representing the correlation between the charge collection efficiency and the fluence or the dose (fig. 6.4, 6.6, 6.8, 6.9), but did not provide satisfactory simple (linear or exponential) interpolation.

The presented analysis was just a preliminary study, the recommendation is to perform a systematic test with more ions type and energy, and increasing the time between the IBIC tests. An interesting result concerns carbon ions is that after 18 days just the ΔE stage seems to recover from the damaging irradiation.

CONCLUSION

Through the presented experimental study three main silicon telescope features were assessed: the transversal and longitudinal definition of the sensitive volume, and the radiation hardness of the device.

The determination of the geometrical characteristics of the sensitive volume of the detector is fundamental for the dosimetric and microdosimetric use, by being the dose and the lineal energy y_i dependent on the length of the path of the ionizing particle and the shape of the sensitive volume.

The experimental investigation provides an estimation of the sample thickness, with satisfactory precision. The detector ΔE stage thicknesses are (1.71 ± 0.07) μm for detector SLAB-OD-1 and (1.95 ± 0.09) for detector SLAB-1D.

In the cross section of the sensitive volume there was evidence of a good uniformity of charge collection efficiency for the part of the sensitive volume that excludes the border. Moreover, the analysis of the border showed border thicknesses not larger than (3.33 ± 0.71) μm for detector SLAB-OD-1 and (0.95 ± 0.25) μm for MICRO-DISKS device. Since the extension of the border is independent on the diameter of the detector cross section, we can extend the results for the border of MICRO-DISKS to all the detectors with identical constructing characteristics and larger diameters.

In typical irradiation conditions, the values of the border thickness allow to estimate the fraction of particles which hit the area of uniform charge collection compared to the particles that hit the border with distorted charge collection. The probability to enter the border zone instead of the uniform zone is about 7 % for the detector SLAB-0D-1, while for MICRO-DISK device the probability to impinge the border zone is higher than the one to enter the uniform area. With the latter case, the border distortion produced on the microdosimetric spectra would be excessive and not recommended. In these conditions and by considering the same border thickness of the MICRO-DISK device, the particles hitting on the border of detector SLAB-0D-1 are less of 3.8 % of those reaching the uniform area.

It is important to stress the fact that the border thickness values derived in this work represent its highest limit.

Finally, the study of the decrease of charge collection efficiency of the silicon telescope due to the accumulated dose from 15 MeV carbon ions and 3.616 MeV silicon ions was performed. By comparing the results of the effect on silicon detector deterioration to the typical dose values adopted in ion-beam therapy, a charge collection efficiency decrease of around 7% for 15 MeV carbon ions is expected when the detector is exposed to a dose corresponding to the full treatment of about two thousand patients (120 kGy). In the case of 3.616 MeV silicon ions which have no clinical relevance, a much higher radiation damage of 19 % is induced.

This project has received funding from the European Union's Horizon 2020 Research and Innovation programme under Grant Agreement no. 654168.

This project has received the support of Luca Tagliapietra and the company Helivertex, which sponsored with travel grants to MedAustron.

REFERENCES

[1] J.L. Helborn, R.W. Sedal, *Lawrence and his laboratory*, University of California Press (1989)

[2] RR. Wilson, *Radiological use of fast protons*, 47:487–91 (1946)

[3] G. Kraft*, Tumor Therapy with Heavy Charged Particles,* Progress in Particle and Nuclear Physics, vs. 45 (2000)

[4] Rossi H.H.,*Specification of radiation quality*, Radiat Res, 10:522 (1959)

[5] International Commission on Radiation Units and Measurements, *The Quality Factor in Radiation Protection (ICRU Report 40),* Bethesda, MD (1986)

[6] International Atomic Energy Agency (IAEA), *Relative Biological Effectiveness in ion-beam Therapy,* Technical reports series no. 461*,* (2008)

[7] A. Wambersie, P. Pichet, H.G. Menzel, *Proton Dosimetry*, 31 (1990) 421

[8] J. Fidorra, J. Booz, *Phys. Med. Biol.*, 26 (1981) 27

[9] J. Fidorra, J. Booz, *Phys. Med. Biol.*, 26 (1981) 43

[10] P.M. Stafford, J.L. Horton, P.R. Almond, *Med. Phys.*, 14 (1987) 1015

[11] International Commission on Radiation Units and Measurements, *Microdosimetry (ICRU Report 36)* ICRU, Bethesda, MD (1983)

[12] D. E. Lea, *Actions of radiation of living cells*, Cambridge University Press (1946)

[13] R. E. Zirkle, D. F. Marchbank, K. D. Kuck, *Exponential and sigmoid survival curves resulting from alpha and x irradiation of* Aspergillus *spores*, J. Cell. Physiol. Suppl. 39 78–85 (1952)

[14] Howard-Flanders, P. Adv. Biol. med. Phys. 6, 553–603 (1958)

[15] Munson, R. J., Neary, G. J., Bridges, B. A. & Preston, R. J. *Int. J. radiat. Biol.* **13**, 205–224 (1967)

[16] H.H. Rossi, M. Zaider, *Microdosimetry and its applications, Springer, New York (1996)*

[17] Y.S. Kim, *Density effect in dE/dx of fast charged particles traversing various biological materials*, Radiat. Res. 1, (1973) 21- 27

[18] G.F. Knoll, *Radiation Detection and Measurement (third edition)*, John Wiley and Sons, New York (2000)

[19] M. Orlic, V. Lazarevic, and F. Boreli, *Microdosimetric Counters Based on Semiconductors Detectors*, Radiat. Prot. Dosim. 29 (1989) 21-22

[20] J.F. Dicello, H.I Amols, M. Zaider, G. Tripard, *A comparison of microdosimetric measurments with spherical proportional counters and solid-state detectors*, Radiat. Res. 82, 441-453 (1980)

[20] A. Kadachi, A. Waheed, and M. Obeid, *Perfomance of PIN photodiode in microdosimetry*, Health Physics 66 (1994) 577-580.

[21] A. Kadachi, A. Waheed, M. Al-Eshaikh, and M. Obeid*, Use of photodiode in microdosimetry and evaluation of effective quality factor*, Nuc. Instrum. Meth. A404 (1998) 400-406.

[22] A.B. Rosenfeld, G.I. Kaplan, M.G. carolan, B.J. Allen, R. Maughan, M. Yudev, C. Kota, J. Coderre, *Simultaneous macro-microdosimetry with MOSFETs*, IEEE Trans. Nucl. Sci. 43(6) (1996) 2693-2700

[23] C.M. Hsieh et al., *A field funnelling effect on collection of alpha-particle-generated carriers in silicon devices*, IEEE Electron Device Letters, EDL-2 (1981) 103-105

[24] S. Agosteo, P.G. Fallica, A. Fazzi, A. Pola, G. Valvo, P. Zotto*, A feasibility study of a solid-state microdosimeter*, Applied Radiation Isotopes, 63 (5-6) (2005) 529-535

[25] S. Gerdung, P.Pihet, J. E. Grindborg, H. Roos, U. J. Schrewe, H. Schuhmacher, *Operation and application of tissue-equivalent proportional counters*, Radiation Protection Dosimetry, Vol. 61, No.4 (1995)

[26] G. Magrin, *Spectra of lineal energy of solid-state detector for ion-beam therapy*, EBG MedAustron internal document, (13th March 2017)

[27] Bhaskar Mukherjee, *LiBe-14, A novel microdosimeter using LiF and BeO thermoluminescence dosimeter pairs for clinical and aerospace applications*, Radiation Measurements 72 (2015) 31-38

[28] P. D. Bradley, A.B. Rosenfeld, M. Zaider, *Solid state microdosimetry*, Nuclear Instruments and Methods in Physics Research B 184 (2001) 135-157

[29] J. F. Zieglar, M. D. Zieglar, J. P. Biersack, Nucl. Inst. Meth. B 268, 1818 (2010)

RINGRAZIAMENTI

Il primo grazie va ovviamente al professor Stefano Agosteo, senza la cui idea e iniziativa questo lavoro non si sarebbe realizzato.

Grazie di cuore a Giulio Magrin, per aver scelto di dedicare questi sei mesi a me e a questo percorso. Grazie per il tempo, la pazienza, i consigli e gli insegnamenti che mi hai trasmesso.

Un ringraziamento va anche al professor Alberto Fazzi, per l'indispensabile contributo alla parte sperimentale su cui si basa questa tesi.

Grazie ai miei genitori, senza l'aiuto e i sacrifici dei quali questi cinque anni di università e questa esperienza austriaca a MedAustron non sarebbero stati possibili.

Grazie ai miei fratelli Greta, Leonardo e Aurora, per aver temprato la mia capacità di concentrazione nelle situazioni più rumorose e caotiche durante questi cinque anni di studio. Forse per ora ho finito.

Grazie al mio meraviglioso cane Musa per l'attento ed interessato supporto nei momenti difficili in cui dovevo ripetere una materia. Sei la mia gioia.

Grazie a Simone, per essere il mio compagno di sogni fin dal primo giorno.

Grazie agli zii Ines, Rosa e Walter, per avermi prestato le stanze più silenziose delle loro case quando c'era un esame da preparare e per le innumerevoli merende. Grazie per l'interessamento costante al mio percorso di studi.

Grazie a Roberta e Federica, per essere amiche sempre presenti, nonostante il tempo che passa e la distanza che ci separa.

Grazie al team "Bergamo scende Lecce", per essere una costante di amicizia da più di cinque anni, nonostante le nostre strade siano cambiate.

Grazie a Sonia, Matteo, Federico, Roberto, Andrea, Roberto e Gregorio, per essere stati i migliori amici che questa laurea magistrale mi potesse regalare. Grazie anche a tutti i compagni di corso e non conosciuti durante questi due anni, per aver reso leggeri e divertenti tutti i giorni di università insieme.

Grazie ad Anna, per aver condiviso con me tutte le gioie e i dolori dell'essere coinquiline fin dal primo giorno a Milano. Grazie anche a Martina, Gloria, Veronica e Deborah, per aver alleggerito la permanenza milanese con cene, uscite, merende e chiacchiere.